QUANTITATIVE OPTICAL SPECTROSCOPY FOR TISSUE DIAGNOSIS

Rebecca Richards-Kortum

The Biomedical Engineering Program, The University of Texas at Austin, Austin, Texas 78712

Eva Sevick-Muraca

School of Chemical Engineering, Purdue University, West Lafayette, Indiana 47907-1283

ABSTRACT

The interaction of light within tissue has been used to recognize disease since the mid-1800s. The recent developments of small light sources, detectors, and fiber optic probes provide opportunities to quantitatively measure these interactions, which yield information for diagnosis at the biochemical, structural, or (patho)physiological level within intact tissues. However, because of the strong scattering properties of tissues, the reemitted optical signal is often influenced by changes in biochemistry (as detected by these spectroscopic approaches) and by physiological and pathophysiological changes in tissue scattering. One challenge of biomedical optics is to uncouple the signals influenced by biochemistry, which themselves provide specificity for identifying diseased states, from those influenced by tissue scattering, which are typically unspecific to a pathology. In this review, we describe optical interactions pursued for biomedical applications (fluorescence, fluorescence lifetime, phosphorescence, and Raman from cells, cultures, and tissues) and then provide a descriptive framework for light interaction based upon tissue absorption and scattering properties. Finally, we review important endogenous and exogenous biological chromophores and describe current work to employ these signals for detection and diagnosis of disease.

INTRODUCTION

It is unimaginable that the manifestation of predisease is not accompanied by some local biochemical change. Whether in culture or intact tissues, predisease

555

biochemistries lead to microscopic structural changes that can influence macroscopic pathology and create the symptoms by which disease is clinically identified. Opportunities to intervene may be enhanced if earlier detection of the prediseased state can be achieved, whether detection is at the biochemical, structural, or (patho) physiological level. Biomedical optics can provide opportunities for diagnosis focusing at each of these levels within intact tissues. In fact, the interaction of light within tissue has been used qualitatively by physicians to aid in recognition of disease since the mid-1800s. The most familiar examples include histology, where stains and dyes are used to provide optical differentiation of cellular structure to yield diagnostic information, and endoscopic procedures, where disease is visually diagnosed on the basis of tissue absorption and scattering.

An excellent example of optical diagnoses based upon biochemistry and structure is the development of optical screening and detection methods for precancer and cancer of the uterine cervix (1). Today, the Pap smear is used to screen the general female population for cervical precancer and cancer in the United States. An abnormal Pap smear is followed by colposcopy where a physician views the cervix by using a magnifying lens to confirm whether precancer or cancer is present. The adoption of these optical screening and detection protocols has dramatically reduced the incidence and mortality of cervical cancer in the United States. Yet the technology still fails in some cases, and in 1995, 15,800 new cases of cervical cancer were reported and 4,800 women died of the disease in the United States (2).

Today's challenge for biomedical optics is to elucidate tissue biochemistry in greater detail and at an earlier stage of disease so that therapeutic interventions may have the greatest impact. As we discuss below, the development of fluorescence and Raman spectroscopy techniques for detection of cervical dysplasia promises to increase the specificity and sensitivity of the test beyond that now available so that mortality rates can be further reduced. The opportunities to broadly apply traditional biochemical optical techniques increase with developments in lasers, laser diodes, fiber optics, and detection technologies. However, owing to the strong scattering properties of tissues, the reemitted optical signal is often influenced not only by changes in biochemistry (as detected by these spectroscopic approaches), but also by physiological and pathophysiological changes in tissue scattering. One challenge of biomedical optical diagnostics is to uncouple the signals influenced by biochemistry, which themselves provide specificity for identifying diseased states, from those influenced by tissue scattering, which are typically unspecific to a pathology. In this review, we briefly describe optical interactions being pursued for biomedical applications and then provide a descriptive framework for light interaction based upon tissue absorption and scattering properties.
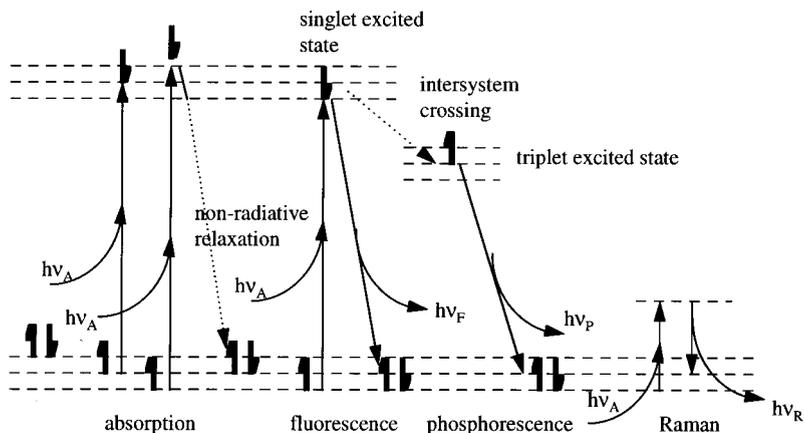
Figure 1   Jablonski diagram detailing the electronic transitions that occur with absorption and with the relaxation resulting in fluorescence and phosphorescence. Raman scattering arises from inelastic scattering associated with alterations in the populations of the vibrational energy levels.

TISSUE OPTICS

Survey of Optical Interactions

Figure 1 illustrates the Jablonski diagram describing the transitions responsible for absorption, fluorescence, and phosphorescence interactions. Following absorption of an excitation photon in the UV-visible region, an activated chromophore is instantly elevated to its excited singlet state, with the electron in the same spin as in its ground state. Relaxation can occur via nonradiative or radiative processes, depending upon the local environment of the molecule. In the radiative processes (fluorescence), the relaxation is accompanied by the release of a reemission photon. For the ideal case of a single activated state and ground state, the mean time between absorption and reemission of the emission photon is known as the fluorescence lifetime, τ. For the typical case in which a fluorophore possesses two or more activated states or populations, there may be several lifetimes reflecting relaxations from different excited states. When there is an intersystem conversion in which the spin of the electron is flipped in the activated energy level, the time for radiative relaxation to the ground state is longer, since return to the ground state must occur with a spin change. This activated state is termed the triplet state, and radiative decay from the triplet state is termed phosphorescence. Tissue absorption, fluorescence, and phosphorescence measurements monitor changes in electronic energy states to provide biochemical information for diagnostics.

Tissue Absorption

In order to obtain biochemical information from a reemitted optical signal, an endogenous or exogenous chromophore is required for interrogation. Endogenous chromophores—such as oxy- and deoxyhemoglobin, melanin, myoglobin, and water—are primarily responsible for absorption of light in the wavelength region of 600–1000 nm, or the "therapeutic window," where tissue scattering predominates over absorption (Figure 2). In the UV and near-UV range, the fluorescent reemission from chromophores such as NAD(P)H, flavins, and porphyrins may provide diagnostic information. However, because of the large absorbance of hemoglobin and myoglobin at wavelengths < 600 nm and the predominant absorbance of water in the IR range (>1000 nm), optical characterization beyond a millimeter of tissue is impractical when outside the therapeutic window of 600–1000 nm. Consequently, back-scattering measurements at these wavelengths ($600 > \lambda > 1000$ nm) characterize surface and subsurface tissues. Typically, values of endogenous tissue absorption coefficients, μ_a range from 0.1 to 10,000 cm^{-1} from the near-infrared (NIR) to UV range, enabling optical penetration from 10 cm to .1 mm before absorption (3).
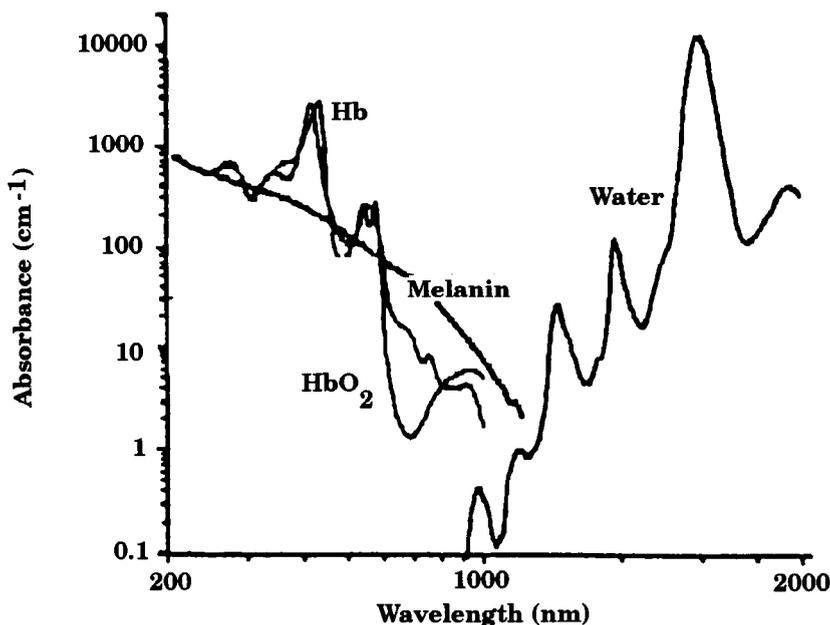

Figure 2   The near-infrared therapeutic window of 600–1000 nm, where tissue absorption is small compared to scattering. [Reproduced from Lim & Soter (280).]

Tissue absorption spectroscopy in transmission geometries depends upon monitoring the attenuation of light in order to determine differences in ground state energies of the chromophore of interest. In nonscattering solutions, attenuation of light over a known pathlength, L, allows prediction of the absorption coefficient, μ_a (cm^{-1}), which is equal to the product of $\epsilon[C]$, where ϵ_i is the extinction coefficient [cm/mM] and $[C_i]$ is the concentration (mM) of chromophore i.

$$\log \frac{I}{I_0} = -\mu_a L = -\epsilon[C]L = -L \sum_i \epsilon_i [C_i]. \qquad 1.$$

Here, I_0 is the illumination intensity, and I is the transmitted intensity.

ENDOGENOUS ABSORBERS   In the NIR range of 750–840 nm, the ground state of oxy- and deoxyhemoglobin provides a variable absorbance for measurement and evaluation of tissue oxygenation. The contributions of chromophores such as cytochrome aa$_3$ and melanin have been reported (4–7), but they are vanishingly small because of the comparatively lower concentrations. In the NIR wavelength region, the extinction coefficient of oxy- and deoxyhemoglobin is typically .1 to .5 cm mM^{-1} (8). Myoglobin can also contribute significantly to tissue absorbance (9). However, since the concentration of oxy- and deoxymyoglobin is not variable in the clinically relevant ranges of tissue pO$_2$, the absorbance due to this chromophore is essentially constant. Water also contributes a constant yet significant background absorbance in tissue (10).

Several research groups and instrument manufacturers have developed NIR instrumentation with multivariate analysis for determining oxyhemoglobin, deoxyhemoglobin, myoglobin, and cytochrome aa$_3$ concentrations in order to assess tissue oxygenation (11). Because the largest optical signal and the early warning danger signs for tissue deoxygenation involve the hemoglobin moieties, the effort to extract spectral features from changing myoglobin and cytochrome may not provide relevant information for the clinical setting. Nonetheless, the analysis seems to provide oxygenation measurements that are usually consistent with physiological status, suggesting that changes in absorption cross section can be measured to provide diagnostics on tissue oxygenation. Indeed, the changes in hemoglobin absorption spectra with oxygenation are the basis of pulse oximetry techniques currently in clinical use (12). Multivariate analysis has also been proposed for IR determination of glucose in tissues and tissue fluids (13). With glucose resonances assigned in the 2.0 to 2.5 μm wavelength regime, the challenge to perform IR tissue spectroscopy for glucose determination is formidable, since water absorption prevents transmission beyond a millimeter of tissue.

EXOGENOUS TISSUE ABSORBERS   NIR absorption measurements can also be used to track exogenous species such as hematoporphyrins or other photodynamic agents whose extinction coefficient in the therapeutic wavelength range can be anywhere from 10 to 100 cm · mM^{-1}, which is much larger than that of endogenous species. Since absorption is due predominantly to the exogenous chromophore, noninvasive measurement of tissue absorption coefficients provides effective measurement of drug concentrations in tissues (14).

However, one daunting difficulty prevents the implementation of the simple Beer-Lambert relationship (Equation 1) for quantitative absorption tissue spectroscopy: The optical path traveled by light through tissues is not a constant, L, since tissue scatters light.

Tissue Scattering

Because of tissue scattering, NIR light can propagate several centimeters, which enables one to extract information noninvasively and deeply. The elastic tissue scattering arises from the microscopic heterogeneities of refractive indices between extracellular, cellular, and subcelluar components. Classical scattering models such as Mie theory or Rayliegh-Debye-Gans approximations depend upon the shape, size-to-wavelength ratio, and refractive index of surroundings and the scattering particles to predict the angular scattering efficiency, Q_{scat} (Ω), and the mean cosine of scatter, $g = \langle \cos \Omega \rangle$ (15, 16) from particulate scatterers. The angular distribution of singly scattered light from bacterial (17) and mammalian cell suspensions (18–20) as well as skin (21) have been predicted successfully by using these classical scattering theories. Tissues are generally forward scattering, with the mean cosine of scattering (or the anisotropy parameter) reported to be between 0.97 and 0.98 (22) and scattering coefficients ranging from 10 to 1000 cm^{-1} (23).

From time-resolved measurements on a blood-free perfused liver, Beauvoit et al (24) determined that the mitochondria provide the predominate component for light scattering of the liver. In these studies, theoretical analyses that assume a randomly distributed mixture of spherical scattering particles of uniform refractive index without interparticle interaction were used to predict $(1 - g)\mu_s$. Predictions showed agreement with measurement on the blood-free perfused liver. Troy et al (25) report tissue scattering properties of human mammary carcinoma and normal breast tissues. Their studies find that the trend of increased scattering coincides with the histopathology of numerous nuclei in these tissues.

The impact of small solutes on the isotropic scattering of yeast suspensions and tissues has also been reported. Using CW measurements, Chance and coworkers (26) demonstrated that small changes in solute concentrations (sodium and potassium chlorides, glucose, mannitol, and sucrose) impact the scattering coefficient by altering the osmotic pressure and thereby cell sizes, and/or by changing the relationship of refractive index between scatterer (the

cell and its components) and its surroundings (27, 28). Using frequency-domain measurements described below, Maier et al (28) monitored the scattering changes of 0.15 cm^{-1} on a human subject following ingestion of 160 g of table sugar. Although opportunities to noninvasively monitor the osmotic or oncotic pressure imbalances through refractive index changes are exciting, these optical property changes can be elicited by a host of physiological responses.

Changes in tissue scattering can also reflect structural changes that are indicative of changes of the physiology or pathophysiology. For example, Saidi et al (21) found that measured increases in the scattering capacity of neonatal skin of varying gestational age can be predicted by Mie theory and by the changes in collagen fiber diameters. From microscopy measurements of fiber concentration and diameter and from integrating sphere measurements of scattering, these investigators calculated the relative refractive index of collagen fibers by using Mie theory. Changes in anisotropy coefficients of the myocardium were predicted by Mie scattering from transmission electron microscopy of protein coagulation (29) and were measured by Bosman (30). Zijp & ten Bosch (31) have modeled the scattering contributions of mineral crystals, collagen fibrils, and dentinal tubules in teeth, and Brinkman et al (32) have reported the capacity of light scattering to detect incipient enamel caries. Endoscopic, multiwavelength measurements of back-scattered light from normal and cancerous bladder also show the capacity to differentiate diseased tissues (33).

Light Transport in Tissues in Vivo: Absorption and Scattering

Not only do the scattering and absorption properties in tissues provide diagnostic information, but they also govern the transport of light through tissues and complicate interpretation of optical measurements. Because of the inhomogeneity of tissues, the solution of Maxwell's equations, which might otherwise be used to model the propagation of light in tissues, is not feasible (34). However, upon ignoring polarization and diffraction effects, the transport of photons through random media (such as tissues) may be modeled as neutral particle transport (35, 36). When the probability for tissue absorption becomes significant (at wavelengths > 600 nm and < 1000 nm), reemitted light is minimally or moderately scattered. In this case, the attenuation of light can be predicted from the Boltzman transport equation (37):

$$\frac{1}{c}\frac{\partial \phi(r, \bar{\Omega})}{\partial t} + \bar{\Omega} \cdot \nabla \phi(r, \bar{\Omega}) + (\mu_a + \mu_s)\phi(r, \bar{\Omega})$$
$$= \int_{4\pi} d\bar{\Omega}' \mu_s(\bar{\Omega}' \to \bar{\Omega})\phi(r, \bar{\Omega}') + S(r, \bar{\Omega}), \qquad 2.$$

which predicts the local angular flux of photons, $\phi(r, \Omega)$, at position r, angle Ω, and time t in a scattering medium. The local absorption coefficient, $\mu_a(r)$, describes the rate of loss of photons at angle Ω, and the local scattering coefficient, $\mu_s(r)$, describes the rate at which photons in direction Ω' are scattered into direction Ω; $S(r, \Omega)$ describes a source term for photons at position r, angle Ω. Equation 2 can be solved subject to appropriate boundary conditions, and its solution can be used to estimate absorption, scattering, and anisotropy from time-independent measurements of transmitted and reflected light intensity with algorithms such as the inverse adding doubling method (38). Alternatively, approximations to the transport equation can be made, as in the case of the Kubelka-Munk theory (39). In yet another approach, Monte Carlo simulations (40) can also predict the photon flux. In these simulations, a computer tracks photon trajectories through tissues. Simulations are carried out using parameters such as the probability of photon transit before absorption or scattering and the probability density function describing scattering direction. Because tens of millions of photon histories must be tracked to statistically simulate physical light propagation, computation times may be excessively long in duration as well as expensive. Recently however, Eddowes et al (41) have used Monte Carlo simulations to show that measurements of coherent back-scattering can be made to determine the optical properties of tissues.

When the probability for absorption is low, as in the case of the NIR therapeutic window, light will be multiply scattered and travel a distribution of optical path lengths before being detected. One can expand the angular flux $\phi(r, \Omega)$ as a sum of Lengendre polynomials (for details see 37), and under conditions in which scattering predominates (i.e. $(1 - g)\mu_s \gg \mu_a$), the expansion can be terminated after the first term. The result is the optical diffusion equation for predicting the angle-independent photon flux, Φ (42):

$$\frac{1}{c}\frac{\partial \Phi(r)}{\partial t} - D\nabla^2\Phi(r) + \mu_a\Phi(r) = S(r). \qquad 3.$$

Here, the optical diffusion coefficient, D, is equal to $3[(1 - g)\mu_s + \mu_a]^{-1}$ and describes the random walk between scattering events as a function of the absorption, μ_a, and isotropic scattering $(1 - g)\mu_s$ coefficients. Equation 3 can be solved for the time variant or invariant fluence to find the intensity reemitted from Fick's law (42):

$$I(r) = -D\nabla\Phi(r). \qquad 4.$$

Upon fitting these transport models to measurements of reemitted light, absorption and scattering properties can be determined. For noninvasive or endoscopic tissue measurements, the tissue of interest is illuminated with a constant intensity source and the back-scattered (reflectance) or transmitted

(transmittance) light is collected. Fiber optic catheters typically provide coupling between tissue and the source and detector. A number of geometries for illumination and detection have been reported that obtain accurate measurements (43–45).

Other investigators have attempted absorption spectroscopy using the Beer-Lambert relationship but using a correction factor describing a mean pathlength, or the differential pathlength factor (DPF), traveled by the propagating photons (46). The mean optical path is determined from time-dependent measurements of light propagation. The simplest measurement consists of launching an incident impulse of light and detecting with picosecond resolution the distribution of photon time-of-flights (47). Upon sampling a statistical number of detected photons with single-photon counting techniques, the distribution is accurately obtained. With the average refractive index of tissue, the mean time-of-flight can be used to compute a mean optical path length. Despite its dependence on absorption and scattering predicted by the diffusion equation (48), investigators have experimentally determined that the DPF is approximately constant in tissues when the separation distance between the source and detector is larger than 25 mm (49).

Alternatively, time-dependent measurements of light propagation in tissues can in themselves provide the most robust information for extraction of tissue absorption and isotropic scattering (50). Measurements can be conducted in both time and frequency domains. In the time domain, an incident impulse of light is launched into tissue and broadens and attenuates because of the tissue optical properties. The broadened pulse of light reemitted from the tissue is fitted to the appropriate solution to the diffusion equation (Equation 3) to obtain measurements of absorption and isotropic scattering (42). Several investigators have developed approaches to quantitatively measure the oxy- and deoxy-hemoglobin concentration in tissues from time-domain approaches (50–52). Noninvasive determination of the local photodynamic agent concentrations is paramount for photodynamic therapy; the product of the local photoactive agent concentration and the local fluence rate governs the cytotoxicity of an effective agent. Investigators have used time-domain reflectance measurements in an in vivo murine tumor model to predict the concentration of hematoporphyrin derivative from the broadening and attenuation of the reemitted pulse of light (53). Pulsed radiometry reflectance measurements have also been employed to monitor exogenous dyes in tissues (54). In this approach, an IR detector is employed to monitor the temperature rise at the tissue-air surface. The temperature difference arises as a result of the absorption that occurs as a pulse of light travels into the tissue. The analysis of absorption and scattering requires proper solution of the diffusion equation coupled with a model for energy transport in tissues.

In frequency-domain measurements, light whose intensity is modulated at Megahertz frequencies is launched into the tissue (48, 55–57). The light that is reemitted is modulated at the same frequency but is phase-shifted and amplitude-demodulated with respect to the incident light. The phase-shift and amplitude demodulation are directly related to the distribution of photon time-of-flights by the Fourier transform and can be used to determine tissue absorption and isotropic scattering coefficients, assuming that multiple scattering occurs (see 48, 58). The instrumentation associated with frequency-domain measurements is considerably less complex than time-domain single-photon counting. Typically, it employs a laser diode whose intensity can be gain-modulated at frequencies up to 1 GHz (59); detection is provided by operating a fast photomultiplier tube (up to 300 MHz) or a multichannel plate (up to GHz) in heterodyne or homodyne modes. With proper phase-locking, the phase-shift and amplitude demodulation can be recovered through simple A/D phase-lock amplifiers, or even network analyzers (60).

In Vitro Tissue Optics: Absorption and Scattering

In vitro measurements of tissue absorption and scattering properties have been previously reviewed by Cheong et al (61) and, as expected, are fraught with artifacts associated with extraction. Viability of tissue, temperature (61), drainage of light-absorbing hemoglobin, and dehydration all impact the optical properties of absorption and scattering. Nonetheless, optical properties of excised tissues are typically acquired in vitro by using measurements of diffuse reflectance and diffuse transmittance with the double integrating sphere apparatus (62). Tissue samples are wetted and placed between two integrating spheres for measurement of diffusely reflected, diffusely transmitted, and collimated light. To obtain values of anisotropy, scattering, and absorption, different models and approximations to the radiative transfer equation can be used to fit measurements to the appropriate values. Kubelka-Munk theory (39) and diffusion theory (35, 36, 63) allow prediction of the isotropic scattering and absorption coefficients, while the inverse adding-doubling method employs the solution of the transport equation to determine anisotropy (38). Frequently, the tissue absorption coefficient is overestimated, owing to light losses in the coupling of samples and integrating spheres (64). Alternatively, these optical parameters can be obtained by matching Monte Carlo simulations of light propagation with actual measurements (65).

FLUORESCENT LIGHT TRANSPORT IN TISSUES

Tissue Optics: Fluorescence

Fluorescence intensity and fluorescence lifetime spectroscopies are well established analytical techniques that can be used to provide chemical sensing

in dilute nonscattering samples (for review, see 66). In tissues, a number of chromophores fluoresce, providing metabolic information. In order to illustrate the problems with fluorescence spectroscopies in tissues, consider first a photon-activated compound that experiences a monoexponential decay of light intensity following an incident impulse of excitation light. In a dilute nonscattering sample, the fluorescent intensity, I_m, and its decay kinetics are defined by the incident intensity, I_0; the extinction coefficient of the chromophore at the excitation wavelength, ϵ; the concentration of probe, $[C(r)]$; the quantum yield at the emission wavelength, α; the lifetime of the probe, τ; and the solution pathlength, L:

$$I_m(t) = I_0 \frac{\epsilon \alpha [C(r)]}{\tau} L \exp\left(-\frac{t}{\tau}\right), \hspace{2cm} 5.$$

where the lifetime of the probe, τ, is defined as the mean time between the absorption of an excitation photon and the reemission of a fluorescent photon. The steady state intensity that results from excitation of the diluted probe is provided by integrating over all reemission times,

$$I_m = \int_0^\infty I_0 \frac{\epsilon \alpha [C(r)]}{\tau} L \exp\left(-\frac{t}{\tau}\right) dt = I_0 \epsilon \alpha [C(r)] L, \hspace{1cm} 6.$$

and is simply a function of the probe concentration, absorption coefficient, and quantum yield. Thus, the reemitted intensity is determined by the local environment of the probe, which may impact ϵ and α, as well as by the local concentration of probe. For ratiometric probes in which reemission is monitored over dual wavelengths [such as bis-carboxyethyl carboxyfluorescein (BCECF)], the ratio of emitted fluorescent intensities is no longer dependent upon the amount of probe available, but only upon the local environment of the probe as detected by the ratio of quantum yields at the two emission or excitation wavelengths:

$$\frac{I_m^{\lambda_1}}{I_m^{\lambda_2}} = \frac{\epsilon^{\lambda_1}}{\epsilon^{\lambda_2}} \frac{\alpha^{\lambda_1}}{\alpha^{\lambda_2}} \neq f([C(r)]). \hspace{2cm} 7.$$

However, when the probe is embedded in a scattering medium, the reemitted intensity for a point source and point detector on the surface of a tissue volume is convolved by probabilities for excitation and emission photon transport. Exogenous ratiometric probes only offer the potential for noninvasive fluorescence intensity spectroscopy independent of probe concentration if differences in tissue optical properties do not differ at the dual wavelengths employed. Thus, ratiometric probes with maximum sensitivity to the metabolite of interest must be designed for a small wavelength window in which tissue absorption and scattering spectra are featureless. Since endogenous probes rarely exhibit ratiometric or isobestic qualities, reemitted fluorescence must be deconvolved from tissue scattering and absorption effects.

CW fluorescence intensity measurements are influenced by the attenuation of excitation and fluorescent light during propagation in tissues. Richards-Kortum et al have developed a simple analytic model that relates the fluorescence of a homogeneous turbid tissue to the concentrations of chromophores that generate intrinsic fluorescence and attenuate excitation and emitted light (67, 68). This model describes the composite tissue spectrum in terms of contributions from fluorophores and absorbers that modulate the intrinsic fluorescence spectrum. Scattering is included empirically by describing absorbers with attenuation spectra that include contributions in both absorption and scattering. Using this model, Richards-Kortum et al have analyzed the fluorescence spectra of normal and atherosclerotic aorta (67, 68).

In the NIR wavelength range, investigators have also employed the diffusion approximation to describe fluorescent properties of tissue phantoms (69–71) from solutions to the coupled diffusion equations describing excitation and fluorescent light propagation in random media:

$$\frac{\partial \Phi_x(\rho, t)}{\partial t} - D_x c \nabla^2 \Phi_x(\rho, t) + (\mu_{a_{x \to m}} + \mu_{a_{x \to}})c\Phi_x(\rho, t) = 0$$

$$\frac{\partial \Phi_m(\rho, t)}{\partial t} - D_m c \nabla^2 \Phi_m(\rho, t) + \mu_{a_{m \to}}c\Phi_m(\rho, t) - \frac{c}{\tau}\alpha\mu_{a_{x \to m}}$$

$$\times \int_0^t \exp\left[-\left(\frac{t - t'}{\tau}\right)\right]\Phi_x(\rho, t')\,\partial t' = 0. \qquad 8.$$

Here subscripts x and m denote the excitation and fluorescent light fluence, c is the speed of light in tissue [$= 3.0 \times 10^{10}$ cm/s$^{-1} \cdot 1.4$ (72)], and $\mu_{a_{x \to}}$ and $\mu_{a_{m \to}}$ are the absorption coefficients for chromophores with nonradiative relaxation at the excitation and fluorescent wavelengths, respectively, and for fluorescent chromophores ($\mu_{a_{x \to m}}$).

A rationale for correcting for the contributions of scatter upon reemission processes has been introduced by Sinaasappel & Sterenborg (73) in order to evaluate the product of fluorescent yield and concentrations in turbid samples illuminated by a CW excitation source. Recently, Hutchinson et al (74) adapted this approach to include time dependence in order to determine lifetimes. In their algorithm, the impact of excitation and emission light propagation is determined by evaluating the probabilities that (*a*) an excitation photon reaches a fluorophore at position *r* at excitation time t' [Φ_x (*r, t'*)] and that (*b*) it activates a probe molecule, which subsequently relaxes yielding a fluorescent photon at time *t**. Because the activation time can vary from time t' to time *t**, the total probability for generating a photon at position *r* at time *t** is obtained by simply integrating over all possible excitation times, t'. Once the fluorescent photon is generated at time *t**, then the probability that it is scattered to the detector

at final time t is given by $[\Phi_m (r, t - t^*)]$. The detected signal at time t that arises from probes contained in volume d^3r is obtained by integrating over all possible reemission times, t^*, across the entire volume (70):

$$I_m(t) = \oint_V \int_{t^*=0}^{t^*=t} \Phi_m(r, t - t^*) \int_{t'=0}^{t'=t^*} \Phi_x(r, t')\alpha[C(r)]$$

$$\times \exp\left(-\frac{t^* - t'}{\tau}\right) \partial t'\, \partial t^*\, \partial^3 r. \qquad 9.$$

The probabilities for excitation and emission light propagation, $\Phi_x(r, t^*)$ and $\Phi_m(r, t - t^*)$ can be determined from Green's functions from the diffusion equation in random media or from appropriate solutions of the radiative transfer equations (depending upon the wavelength range and the optical properties of tissues). Because $\Phi_x(r, t^*)$ and $\Phi_m(r, t - t^*)$ are functions of the absorption and scattering properties of the tissue or media, determining lifetime, quantum yield, or concentration of fluorophore is difficult without prior measurement. Indeed, for CW or time-invariant fluorescence measurements, an added integration over all possible times further makes the inverse problem intractable:

$$I_m = \int_{t=0}^{t=\infty} \oint_V \int_{t^*=0}^{t^*=t} \Phi_m(r, t - t^*) \int_{t'=0}^{t'=t^*} \Phi_x(r, t')\alpha[C(r)]$$

$$\times \exp\left(-\frac{t^* - t'}{\tau}\right) \partial t'\, \partial t^*\, \partial^3 r\, \partial t. \qquad 10.$$

In the case of Raman spectroscopy, when reemission processes are considered spontaneous, the problem is made simpler by changing the order of integration:

$$I_m = \oint_V \alpha[C(r)] \int_{t=0}^{t=\infty} \int_{t^*=0}^{t^*=t} \Phi_m(r, t - t^*) \int_{t'=0}^{t'=t^*} \Phi_x(r, t')\, \partial t'\, \partial t^*\, \partial t\, \partial^3 r$$

$$\sim \oint_V \alpha[C(r)]\Phi(r)\, d^3 r$$

$$\sim \alpha[C] \oint_V \Phi(r)\, d^3 r. \qquad 11.$$

where the term $\Phi(r)$ denotes the contribution of excitation and emission propagation over all possible combination of times. If the wavelengths of excitation and emission are in the NIR range, then $\Phi(r)$ can be determined from the diffusion equation(s). Otherwise, the Boltzman equation or the solution of Maxwell's equations for single cells is necessary. Equation 11 shows that if the yield and concentration are independent of spatial position and if the contributions of emission and excitation propagation at the wavelengths employed are identical, the dual-wavelength measurements provide information on wavelength-dependent yield.

In order to extract the intrinsic fluorescent intensity or intrinsic fluorescence lifetime for identification of endogenous probe concentration and quantum yield, a priori information about tissue absorption and scattering optical properties must be obtained. Although noninvasive measurements of tissue absorption and scattering are possible from CW (continuous wave) and time- and frequency-resolved measurements, they nonetheless may not describe the heterogeneities in absorption and scattering that can impact the intensity and time dependence of reemitted fluorescence. Monte Carlo methods (described below) can describe the effects of heterogeneities.

A detailed analysis of the dependence of the fluorescence line shape and intensity of excitation and collection geometry was presented by Keijzer et al, who developed a Monte Carlo model that simulated the propagation of excitation and fluorescent photons in a multilayer tissue with the optical properties of normal human aorta (75). This simulation includes the effects of the excitation beam profile, local variations in index of refraction, and optical properties within the sample and varying collection geometries, and is based on the convolution of the excitation beam profile with the fluorescence escape function for a point source located within the tissue samples. Using this formalism, it is possible to explore the relative contributions of sources at various locations in the tissue to the fluorescence spectrum and to study the effects of varying excitation and collection geometries.

Endogenous Tissue Fluorophores

Endogenous fluorescence provides an important tool in optical assessment of tissue metabolic status. The pyridine nucleotides and the flavins play an important role in cellular energy metabolism (76). Nicotinamide adenine dinucleotide is the major electron acceptor (Figure 3); its reduced form is NADH, and the reduced nicotinamide ring is fluorescent (Table 1) (66). Reduced pyridine nucleotide (RPN) fluorescence has been measured in solution, in mitochondria (77), in intact cells (78), and in whole tissues (79). Both the excitation and emission maxima of RPN are blue-shifted upon binding to dehydrogenases (80). The fluorescence quantum yield of NADH increases approximately four-fold when bound to proteins (66). Flavin adenine dinucleotide is the other major electron acceptor; the oxidized form, FAD, is fluorescent, while the reduced form, $FADH_2$, is not (Table 1) (81). Several investigators have shown that when excited in the near-UV region, the endogenous fluorescence near 500 nm is reduced in tumor tissue relative to normal surrounding tissues. The differences may lie in the decrease in the oxidized forms of flavins and the relative amount of NADH in malignant tissues.

Masters & Chance (81) have described a method to map the redox state of tissues in three dimensions by using confocal fluorescence imaging to measure the intrinsic fluorescence probes that report on cellular metabolism: NAD(P)H
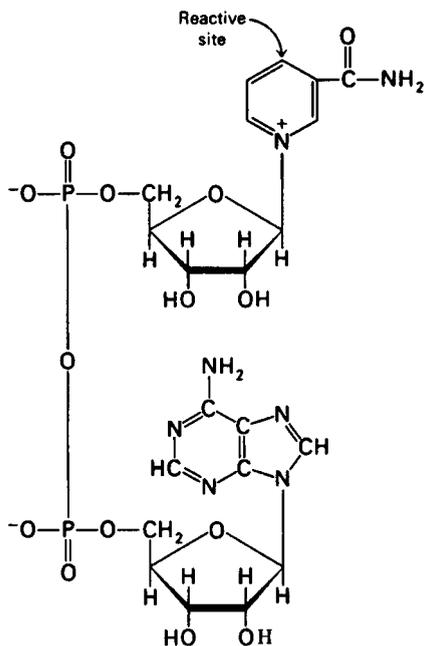
Figure 3   The pyridine nucleotides play an important role in cellular energy metabolism. The oxidized form of nicotinamide adenine dinucleotide, shown here, is a major electron acceptor; its reduced form is NADH, and the reduced nicotinamide ring is fluorescent. (Adapted from Reference 76.)

and the oxidized flavoproteins. The basis of this technique is that the quantum yield of NAD(P) is higher for the reduced form and lower for the oxidized form, whereas the opposite is true for the flavoproteins (81). By measuring the ratio of fluorescence intensity of these two chromophores with a confocal fluorescence microscope, a physical map corresponding to the local redox state of the tissue can be created (81).

The aromatic amino acids, tryptophan, tyrosine, and phenylalanine, contribute to protein fluorescence (Table 1) (66, 82). At excitation wavelengths above 295 nm, only tryptophan is excited (66). From 280 to 295 nm, both tyrosine and tryptophan are excited; however, energy transfer from tyrosine to tryptophan is quite common (66). Below 280 nm, all three aromatic amino acids can be excited; however, the quantum yield of phenylalanine is relatively low compared to that of tryptophan and tyrosine (66).

Fluorescence has been noted in the structural proteins collagen (83) and elastin (84). Collagen and elastin fluorescence is associated with cross-links

**Table 1**   Endogenous fluorophores at physiologic pH

Chromophore	Absorption maxima	Molar extinction coefficient	Excitation maxima	Emission maxima	Fluorescence quantum yield
HP, collagen, elastin	325 nm (83)		325 nm (83)	400 nm (83)	
LP, collagen, elastin			325 nm (86)	400 nm (86)	
Collagen powder			280 nm, 265 nm, 330 nm, 450 nm (88)	310 nm, 385 nm, 390 nm, 530 nm (88)	
Elastin powder			350 nm, 410 nm, 450 nm (88)	420 nm, 500 nm, 520 nm (88)	
Tryptophan	280 nm (82)	5.6×10^{-3} (82)	280 nm (66)	350 nm (82)	0.2 (82)
Tyrosine	275 nm (82)	1.4×10^{-3} (82)		300 nm (82)	0.1 (82)
Phenylalanine	260 (nm) (82)	2×10^{-4} (82)		280 nm (82)	0.04 (82)
Pyridoxine (PN)	324 (94)		332 (94)	400 (94)	
Pyridoxal (PL)			330 (94)	380 (94)	
Pyridoxamine (PM)	326 (94)		335 (94)	400 (94)	
Pyridoxal 5′-phosphate (PLP)			330 (94)	400 (94)	
4-Pyridoxic acid (PA)	307 (94)		315 (94)	425 (94)	
NADH	260 nm 340 nm (82)	14.4×10^{-3} 6.2×10^{-3} (82)	290 nm (77) 340 nm (66)	440 nm (77), 450 nm (66)	
NAD+	260 (82)	18×10^{-3} (82)			
FAD			450 nm	515 nm	
Ceroid			340–395 nm (97, 102)	430–460 nm, 540–640 nm, (97, 100, 102)	
Lipofuscin			340–395 nm (97, 102)	430–460 nm, 540–540 nm, (97, 100, 102)	
Eosinophils—circulating			370 nm, 500 nm (107)	440 nm, 550 nm (107)	
Eosinophils—granules			380 nm, 450 nm (108, 109)	520 nm (108, 109)	

(83, 85). In elastin, two major types of cross-links are the unique amino acids desmosine and isodesmosine (86). In collagen, it is believed that there are two pathways for cross-link formation: one important in skin and the other important in load-bearing tissues. In load-bearing tissues, two types of cross-links are found: hydroxylysyl pyridinoline (HP), and lysyl pyridinoline (LP) (86). Their structures are shown in Figure 4a. Both HP and LP are autofluorescent with an excitation maximum at 325 nm and an emission maximum at 400 nm (83, 86); the excitation and emission spectrum of each are shown in Figure 4b. Although desmosine was initially believed to be responsible for elastin autofluorescence, Thornhill showed that desmosine could be separated from the fluorescent material in elastin (85). Further work has indicated that the fluorescent material in elastin is due to a tricarboxilic, triamino pyridinium derivative, which is very similar to the fluorophore in collagen (87). The excitation and emission maximum of this elastin cross-link is shown in Figure 5; again, the excitation maximum is at 325 nm, and the emission maximum is at 400 nm.

Richards-Kortum et al (88) measured the fluorescence of powdered bovine collagen and elastin over the UV and visible regions of the spectrum. Excitation and emission maxima for collagen were observed, respectively, at 280 and 310 nm, 265 and 385 nm, 330 and 390 nm, and 450 and 530 nm. The peak at 330 and 390 nm correlates well with the spectrum of LP shown in Figure 4. The molecular origin of the other peaks has not been explored. Elastin powder had excitation and emission maxima at 350 and 420 nm, 410 and 500 nm, and 450 and 520 nm, respectively. Although none of these maxima correspond with those observed by Deyl et al (87), when the elastin powder was excited at 325 nm, the resulting emission maximum was at 400 nm. Again, the molecular origin of these peaks has not been explored. The reduction in autofluorescence attributed to collagen at 390 nm in spectra of malignant tissues may be due to the tumor specific collagenase (89, 90) and the loss of collagen content.

Pyridoxine (vitamin B_6) and its derivative, pyridoxal 5′-phosphate, are required by many of the enzymes involved in amino acid metabolism (91). Several diseases are associated with defects in vitamin B_6 metabolism, including celiac disease, cirrhosis, renal disease, and cancer (92, 93). All of the vitamin B_6 metabolites exhibit autofluorescence, with an excitation maximum near 330 and an emission maximum near 420 nm (94).

Several groups have identified fluorescent pigments in tissues associated with aging (95–97) and various pathological processes, such as atherosclerosis (98, 99) and retinal degeneration (97, 100, 101). These pigments are associated with lipid oxidation products and have been termed lipopigments. There appear to be two closely related types of lipopigments: ceroid and lipofuscin (102). Lipofuscins are pigmented granules that are 1–5 μm in diameter and found
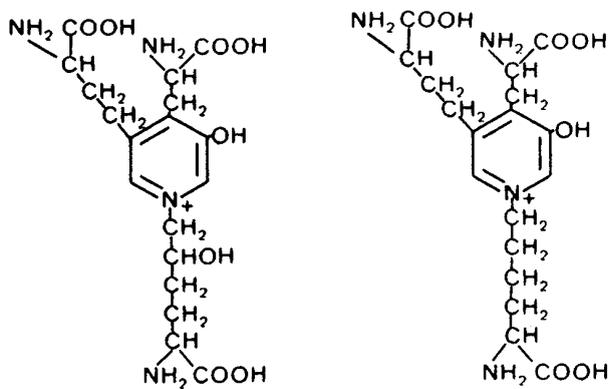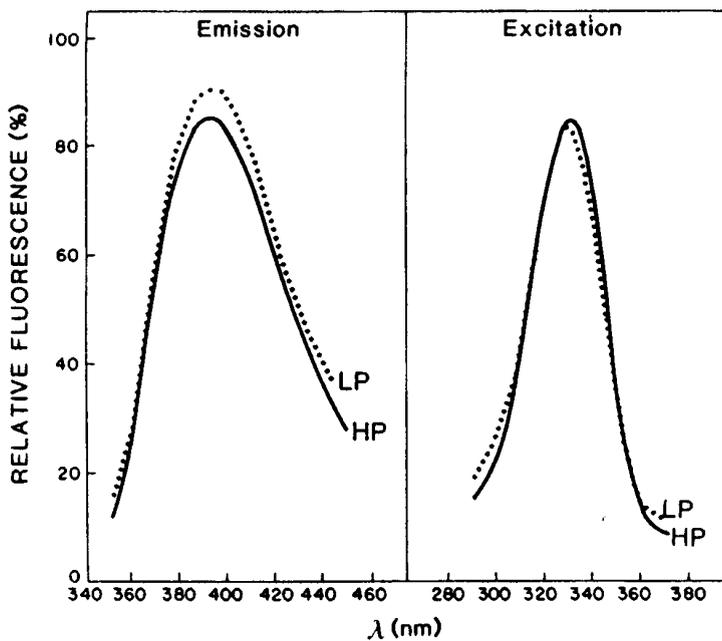
Figure 4 (*a*) Structures and (*b*) excitation and emission spectra of HP and LP. (Adapted from Reference 86.)

within the cytoplasm of postmitotic, metabolically active, long-lived cells such as neurons and cardiac myocytes. Similar structures, formed in response to pathological conditions such as vitamin E deficiency, have been termed ceroid; ceroid may be an early stage of lipofuscin (102). Lipofuscin granules are believed to be the end product of lipid peroxidation (97) and to contain damaged cell membranes that have been phagocytized during the life of the cell (100). Both ceroid and lipofuscin emit an intense yellow-orange autofluorescence when illuminated with UV excitation in situ in histological sections (102). The excitation maxima of in situ and isolated granules have been reported to range from 340 to 395 nm; there are two emission maxima, the first from 430 to 460 nm, the second from 540 to 640 nm (102). Figure 6 shows corrected
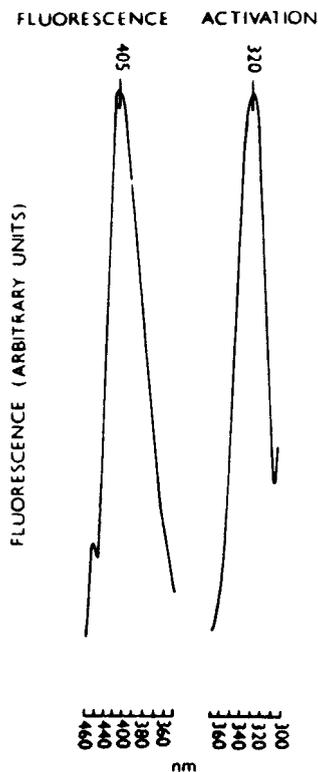
Figure 5   The excitation and emission spectra of the elastin cross-link. The emission (fluorescence) spectrum was measured at 320-nm excitation; the excitation (activation) spectrum was measured at 405-nm emission. (Adapted from Reference 87.)
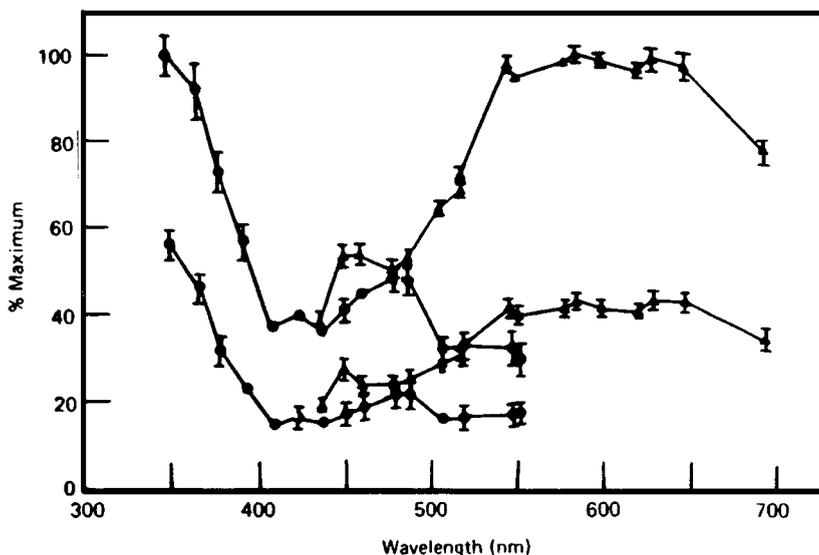
Figure 6   Corrected excitation and emission spectra from in situ lipofuscin granules in young and old retinal pigment epithelium (RPE). Upper lines represent data from old tissue; lower lines represent data from young tissue. Excitation spectra are for emission greater than 570 nm. (Adapted from Reference 104.)

excitation and emission spectra from in situ lipofuscin granules in young and old retinal pigment epithelium (RPE) (100). As the RPE ages, the fluorescence intensity increases, particularly in the orange-yellow region of the spectrum. These results are consistent with the visual observations of fluorescence of lipopigments in situ (100, 101). Many studies of the fluorescence of material extracted from lipofuscin-rich tissues have indicated only a single emission maximum in the blue, near 430–460 nm (95, 103). Stark, Eldred, and coworkers point out that this finding may be due to the markedly decreasing response of most spectrofluorimeters in the red; most studies of lipofuscin fluorescence have reported raw data that are uncorrected for the wavelength-dependent spectral response of the spectrofluorimeter (100, 101). The chemical compositions of the chromophores of ceroid and lipofuscin are not well understood (104).

Eosinophils (EOs) are one of the three types of white blood cells that form an important component of the nonspecific immunological defense system of the human body (105, 106). EOs contain diagnostic large eosinophilic granules, are birefringent, and are intensely fluorescent (107–111). As viewed through the fluorescence microscope, the fluorescence of fixed circulating EOs (109),

fixed EOs in bone marrow (111), and unfixed EOs in tissue sections (107) is associated with cytoplasmic granules and is a bright yellow when excited with 500-nm radiation. Upon UV excitation, EOs in tissue sections also fluoresce with an amber gold color (107). However, the fluorescence of unfixed EOs from circulating human blood appears blue upon UV excitation (107). Similar differences are also seen in the fluorescence spectra of EOs. Weil & Chused reported fluorescence spectra of eosinophilic granules isolated from human blood with excitation maxima at 370 and 450 nm and with an emission maximum at 520 nm (109). This was confirmed by Mayeno et al (108), who reported excitation maxima at 380 and 450 nm, with emission maxima from eosinophilic granule extracts at 520 nm. They demonstrated that this fluorescence is due to FAD, and suggested that the granule-associated flavoproteins may act as a source of hydrogen peroxide and/or superoxide, which in conjunction with EO enzymes could yield potent cytotoxic enzymes (108). Barnes et al (107) measured the fluorescence excitation emission matrices of intact, unfixed EO isolated from human blood and noted two excitation emission maxima: one with an excitation peak at 370 nm and an emission maximum at 440 nm, the other with an excitation maximum of 500 nm and an emission maximum of 550 nm. This finding was consistent with the blue fluorescence observed from circulating, unfixed EOs under UV illumination but differed dramatically from that obtained from eosinophilic granule extracts and measurements made in tissue sections. Barnes et al hypothesized that the fluorescence of eosinophils may be site dependent (107).

Red fluorescence of necrotic tumors was noted as early as 1924 in a study of four rat sarcomas (112). Ronchese et al (113) demonstrated in 1954 that this red fluorescence was specific for advanced ulcerated squamous cell carcinoma; was not found in ulcers, warts, or other ulcerated and nonulcerated benign and malignant cutaneous diseases; and thus could be of use diagnostically. The specificity of the red fluorescence was confirmed in 1960 by Ghadially, who ascribed the red fluorescence to porphyrins (114). Ghadially & Neish subsequently showed that the red fluorescence was due to protoporphyrin (115). The origin of the protoporphyrin in ulcerated squamous cell carcinomas was ascribed to several sources. Ghadially suggested that it was a product of microbes or of the tumor itself or was removed from the blood stream and excreted by the tumor (114). Sharvill argued against a bacterial origin, as organisms cultured from fluorescent tumors failed to show red fluorescence in culture (116). However, Ghadially et al later showed definitive evidence for a bacterial origin (117). Tumors injected with Staphylococci or coliform bacilli produced red fluorescence, although these organisms did not produce red fluorescence when grown in normal culture media. Ghadially et al (117) concluded that the host

must supply some factor necessary for the production of red fluorescence that was not present in the culture medium. He subsequently showed that these bacteria would produce red fluorescence when grown in culture medium containing delta-amino-laevulonic acid, a precursor to protoporphyrin.

Diagnostic Uses of Steady State Fluorescence Spectroscopy

The primary clinical applications of fluorescence spectroscopy for tissue diagnosis have been for atherosclerosis and neoplasia. Work in these fields has been recently surveyed (118, 119).

ATHEROSCLEROSIS   Edholm & Jacobson (120) suggested that quantitative optical techniques could be used in vivo to improve the diagnosis of atherosclerosis; they measured reflectance of the aorta at 500 and 550 nm in 15 patients undergoing aortography. Kittrell et al (121) suggested that optical diagnosis and therapy for atherosclerosis could be combined in a single-fiber optic device and demonstrated that fluorescence spectroscopy could be used to discriminate between normal aorta and fibrous plaque with an intimal thickness greater than 0.5 mm in vitro (Figure 7).

Subsequent to Kittrell's work, several groups have investigated the utility of fluorescence spectroscopy for the diagnosis of atherosclerotic plaque, many with the goal of developing a guidance system for laser angiosurgery catheters. The fluorescence of normal and atherosclerotic plaques has been measured as a function of excitation and emission wavelength over the entire UV and visible region of the spectrum (88, 122–125).

Small changes in the excitation wavelength ($< \pm 20$ nm) used to obtain arterial spectra do not result in large changes in the emission spectrum, except in the region from 306 to 310 nm. Here, three peaks are noted in the emission spectrum of normal aorta at 335, 380, and 440 nm, with the intensity of the peak at 335 nm decreasing as the excitation wavelength increases (Figure 8*a*) (126). When emission spectra were obtained at 306- to 310-nm excitation from a section of normal aorta that was optically thin so that reabsorption effects would be negligible, only two peaks were observed at 335 and 380 nm; Baraga (126) attributes the valley at 418 nm to reabsorption of tissue fluorescence by oxyhemoglobin, and attributes (Figure 8*b*). The peak at 380-nm emission was attributed to a combination of collagen and elastin fluorescence (126).

The morphological basis for discrimination of normal artery and atherosclerotic plaques based on fluorescence emission has been investigated (127, 128). At both 350- and 476-nm excitation, the autofluorescence of normal vessels was largely due to collagen and elastin. Atheromatous plaques had intensely

fluorescent ring-shaped or discrete solid deposits in the necrotic core. The intensity of these deposits was highly variable, and the color of fluorescence was yellow, with both UV and visible excitation (127, 128). These deposits stained positively with lipid stains, but they could not be extracted with alcohols and were thus identified as ceroids (128).

The choice of excitation wavelength determines which fluorophores can contribute to the arterial emission spectrum in two ways: First, only those chromophores that absorb at the excitation wavelength can be excited; and second, only those chromophores contained in tissue layers to which excitation light penetrates and from which emission light can escape the tissue surface will produce fluorescence that can be measured from the tissue surface (129). A simple model has been presented that predicts the depth of tissue responsible
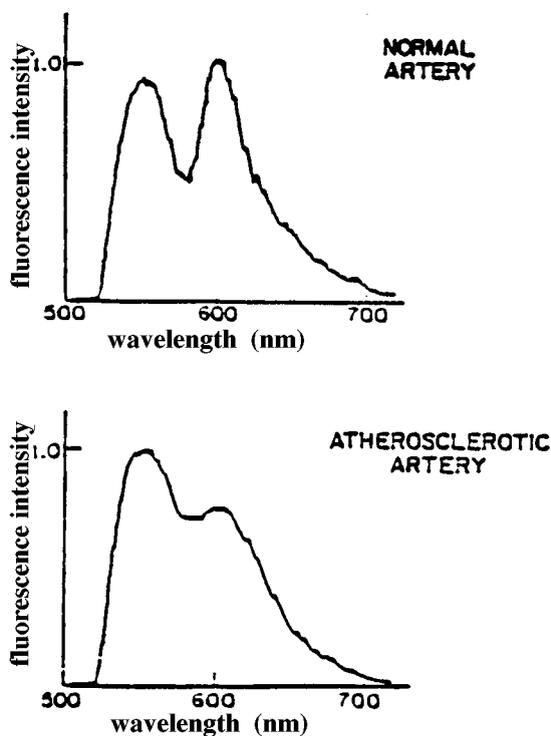
Figure 7 Fluorescence emission spectra of normal and atherosclerotic aorta at 480-nm excitation. The intensity of the peak at 600 nm was lower in fibrous plaque than in normal aorta, and the ratio of the intensity at 600 nm to that at 580 nm was significantly lower in fibrous plaques than in normal tissues ($p < 0.01$). (Adapted from Reference 121.)
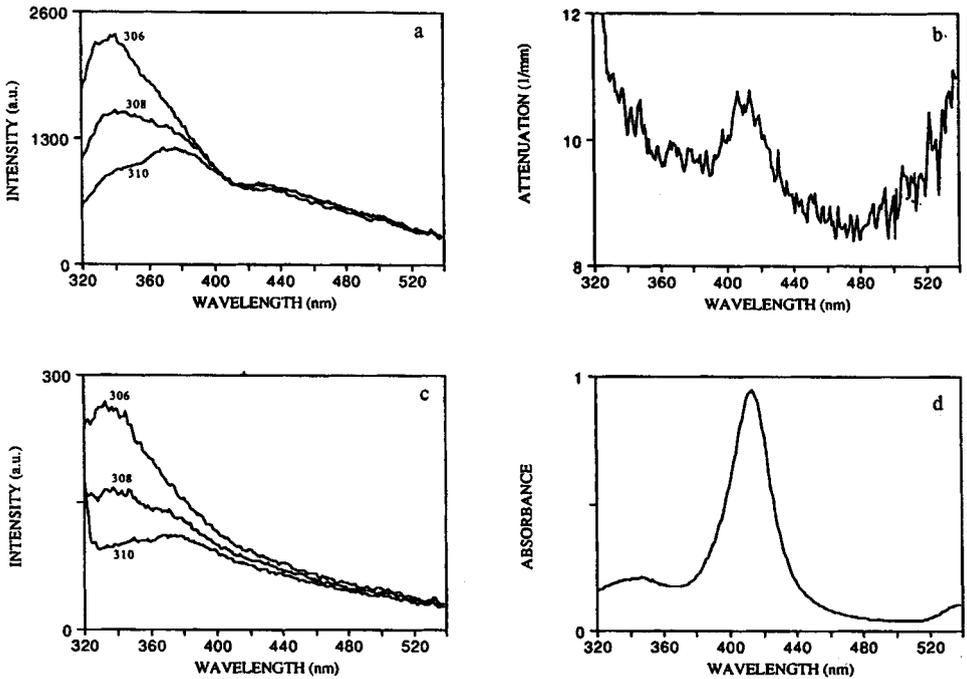
Figure 8   (*a*) Fluorescence emission spectra of intact arterial tissue from 306- to 310-nm excitation. (*b*) The attenuation spectrum of arterial intima has a peak attenuation at 420 nm. (*c*) The emission spectra at 306- to 310-nm excitation from a section of normal aorta which was optically thin so that reabsorption effects would be negligible shows only two peaks at 335 and 380 nm. (*d*) Baraga et al (126) attributes the valley at 418 nm to reabsorption of tissue fluorescence by oxyhemoglobin and attributes the peak at 380-nm emission to a combination of collagen and elastin fluorescence (126). (Adapted from Reference 126.)

for generating 95% of the fluorescence emitted from the tissue surface as a function of sum of the attenuation coefficients at the excitation and emission wavelengths (129). Gmitro showed that at 325-nm excitation, this model accurately predicted the depth dependence of tissue fluorescence in normal and atherosclerotic artery and that 95% of arterial fluorescence was produced by the top 150 μm of artery (129).

Several groups have examined the utility of fluorescence emission spectra obtained at 308-nm excitation for use in diagnosing early- (130) and late-stage atherosclerosis (126) in vitro. Emission spectra of fatty streaks at 308-nm excitation are red-shifted and spectrally broader than spectra of normal aorta, with a peak at 430 nm and a FWHM of 170 nm (130). Oraevsky et al (130) attribute this spectral change to the accumulation of oxidized low-density lipoproteins

in the intima of fatty streaks. In atheromatous (fibrofatty) plaques, a decrease in the intensity of the tryptophan peak is seen (126), although the exact peak location and width seem to vary (130). Normal aorta can be separated from atherosclerotic plaque with a positive predictive value of 93% for 60 samples based on intensity ratios (126). Baraga et al (126) note that other studies at 325- or 337-nm excitation, where tryptophan is not excited, have been unable to differentiate normal aorta and ulcerated calcified plaques (124) and suggest that excitation at 308 nm avoids this problem.

Leon et al (124) described qualitative changes in the spectra of aorta and coronary arteries at 325-nm excitation. At this excitation wavelength, all tissues showed a single peak, with maximum intensity near 465 nm. Atherosclerotic samples showed on average a 45% reduction in absolute fluorescence intensity, and normalized fluorescence spectra showed increased peak area, increased peak width, and higher intensities at ± 40 nm and $+ 80$ nm from the fluorescence maximum in the spectra of atherosclerotic samples. At 325-nm excitation, Gaffney et al (131) showed that features of the fluorescence emission spectrum acquired in vitro are correlated to the maximal intimal thickness and to the portion of the atherosclerotic lesion occupied by fat, calcium, and fibrotic tissue. Gaffney et al (131) noted that correlations to a large range of intimal thicknesses (0.25 to 4 mm) could be achieved, despite the fact that these thicknesses greatly exceed the depth of tissue that can be probed using fluorescence spectroscopy at this excitation wavelength (129).

The biochemical basis for the difference between 325-nm excited fluorescence spectra of normal aorta and atherosclerotic plaques has been investigated (132). Laifer et al (132) fit normalized spectra of 91 normal and 91 atherosclerotic samples to a linear combination of normalized collagen and elastin fluorescence and then extracted the relative contribution of each chromophore; the average elastin coefficients were greater for normal aorta than for atherosclerotic tissue, and the difference was used to classify tissue type as normal or atherosclerotic with 90% accuracy in a prospective setting.

Gindi et al (133) compared the ability of several different types of classifiers based on 325-nm excited fluorescence emission spectra in order to develop algorithms for discriminating normal tissue and atherosclerosis in both aorta and coronary artery. The accuracy of classification was compared for classifiers derived using back-propagation neural networks, K nearest neighbor classifiers, multivariate and step-wise multivariate linear regression, principal component analysis, decision plane analysis, principal peak ratio, Bayes theorem, and spectral width. In all cases classification accuracies were lower for coronary artery than for aorta; otherwise all methods performed with reasonably similar accuracy (133).

Deckelbaum et al (134) showed that normal and atherosclerotic arterial fluorescence spectra could be collected in vivo with good signal-to-noise ratios in a rabbit model at 325-nm excitation. The fluorescence of blood could easily be differentiated from that of artery based on its much lower fluorescence intensity, and spectra of artery could be obtained in a blood field, provided the residual layer of blood between the tissue and the catheter tip used to record in vivo spectra did not exceed 50 μm in thickness (134).

Using 337-nm excitation, Deckelbaum et al (135) obtained emission spectra qualitatively similar to those obtained with 325-nm excitation. Deckelbaum et al (135) suggested that carotenoids, which have been reported to fluoresce at 538 nm (136), could be partly responsible for the fluorescence of yellow plaque.

At 458- and 476-nm excitation, arterial spectra show three peaks at 520, 550, and 600 nm (137, 138). In general, normal aorta spectra exhibit 520- and 600-nm peaks of greater intensity relative to the 550-nm peak, and normal aorta spectra also exhibit better defined valleys between all peaks (137, 138). These peaks are generated through a combination of intrinsic fluorescence of collagen, elastin, and ceroid, with reabsorption of fluorescence by oxyhemoglobin (67, 68). Absorption maxima of heme are present at 540 and 580 nm. These peaks modulate the intrinsic fluorescence of the tissue and produce valleys at 540 and 580 nm in the tissue fluorescence spectrum (67, 68). The fluorescence intensity of noncalcified atherosclerotic plaques is less than that of normal aorta but greater than that of normal coronary artery at 476-nm excitation (138); the fluorescence intensity of calcified plaques is greater than that of normal aorta at 458-nm excitation (137), and is greater than that of both normal aorta and coronary artery at 476-nm excitation (138). Sartori et al (137) showed that calcified atherosclerotic plaques could be mapped out in aorta by using a scanning fiber optic device to sample the fluorescence intensity as a function of spatial position.

Using a model, Richards-Kortum et al have analyzed the fluorescence spectra of normal and atherosclerotic aorta (67, 68) and coronary artery (139). In aorta, the structural protein fluorescence contribution decreases and the ceroid contribution increases as tissue becomes atherosclerotic. 88% of samples could be correctly classified by using an algorithm based on the structural protein contribution and ceroid contribution (68). Eighty-two samples of coronary artery could be classified as normal, noncalcified plaque, or calcified plaque by using similar parameters with 92% overall accuracy.

Richards-Kortum et al (140) showed that fluorescence spectra could be obtained from arterial tissues by using optical fiber probes; results were similar to those obtained using conventional lenses to couple light into the spectrometer,

provided that the collection and delivery geometries of the two systems are equivalent. The interaction of absorption and fluorescence, which determines the fluorescence line shape of arterial tissue, implies that the measured line shape depends on the geometry of the excitation and collection optics used to record the fluorescence spectrum, and suggests that algorithms designed for a particular collection system may be valid only for that system (140). As the area of tissue from which fluorescence is collected is increased to be larger than that directly illuminated by excitation light, the effects of reabsorption on the spectrum become greater (valleys at 540 and 580 nm become deeper) (140). The most useful delivery-collection geometry is one that yields spectra that are independent of such geometric dependencies (140). Richards-Kortum et al have argued that this occurs if fluorescence is collected only from the area of tissue that is directly illuminated (140).

Hoyt et al (141) demonstrated that fluorescence spectral maps could be measured from the interior of an intact artery in vitro by using a multifiber catheter that obtained complete emission spectra with 500 μm resolution. These spectral maps were used to determine whether each fiber in the catheter viewed normal aorta, atherosclerotic plaque, or blood with good accuracy compared to traditional histopathological analysis (141). Warren et al showed that 476-nm excited fluorescence spectral images could be obtained from intact coronary arteries (142). When intravascular ultrasound measurements were made simultaneously, the fluorescence data could be calibrated for variations in the tissue catheter separation, and the resulting processed data could be used to determine the spatial distribution of structural protein and ceroid and the presence of non-calcified and calcified atherosclerotic plaque with good accuracy compared to histology and ultrasound images (142).

Much of the motivation to develop fluorescence-based methods for the detection of atherosclerotic plaque has been to develop a guidance system for laser angiosurgery catheters that can decrease the complication of perforation. Several groups have investigated the effects of exposure to high-power laser light on the fluorescence spectra of arterial tissues (124, 126, 143, 144, 145). Chaudhry et al (143) showed that subablation fluences of light could induce significant photobleaching. Leon et al (124) showed that as atherosclerotic tissue was ablated with argon, excimer, or 480-nm light from a pulsed dye laser, the fluorescence intensity of the crater at 325-nm excitation increased to approximately that of normal tissue when the residual intimal thickness was less than 200 μm.

FLUORESCENCE-BASED DIAGNOSIS OF NEOPLASIA   An early report suggesting that quantitative fluorescence spectroscopy could be used to discriminate normal and malignant tissues appeared in 1965 (146). Emission spectra were recorded

at 330-nm excitation from excised normal tissue and tumors of the esophagus, stomach, breast, and thyroid. All tissues showed emission in the range from 360 to 600 nm, which was similar to that of tryptophan; the fluorescence intensities of cancerous tissues were less than those of normal tissue from the same patient (146). Lycette & Leslie (146) suggested that some of the observed differences might be due to tumor necrosis and could be useful diagnostically. In the 1980s, it was again suggested that fluorescence spectroscopy might be useful for tissue diagnosis. Alfano et al (147) measured fluorescence spectra from cancerous and normal rat kidney and prostate tissues and normal and cancerous mouse bladder tissues at 488-nm excitation in vitro. They observed differences in the spectral profiles of both normal and cancerous tissues as well as blue-shifting of the primary peak in the spectrum of cancerous tissues relative to that of normal tissue (147). Alfano et al attributed tissue fluorescence to flavins and porphyrins and suggested that differences in spectra were caused by different environments in the two types of cells (147). Yuanlong et al surveyed the fluorescence spectra of normal and cancerous tissue from various organ sites at 365-nm excitation in vitro (148). Cancerous tissues exhibited emission peaks at 630 and 690 nm that were not observed in the fluorescence spectra of normal tissues; these peaks were attributed to naturally occurring porphyrins (148). On the basis of these peaks, 89% of 50 specimens of stomach, esophagus, tongue, mandible, and bladder could be classified as normal or cancerous in agreement with histological analysis (148).

Based on this early work, several groups have investigated the use of fluorescence spectroscopy for the diagnosis of cancers and precancers in extensive in vitro and in vivo studies. Results are reviewed here by organ site.

The use of fluorescence spectroscopy for identification of colonic neoplasms has been recently reviewed (119). Richards-Kortum et al (149) investigated whether fluorescence spectroscopy could be used to discriminate between normal and adenomatous (precancerous) colon tissue in vitro, surveying fluorescence emission at a number of excitation wavelengths spanning the UV and visible spectrum. They found that excitation at 330, 370, and 430 ± 10 nm yielded the greatest differences between the fluorescence of normal and adenomatous colon (149). Kapadia et al (150) showed that UV-induced (325 nm) fluorescence emission spectra could be used to discriminate adenomas from normal tissue and hyperplastic polyps with 94–100% accuracy in an algorithm based on stepwise multivariate linear regression tested prospectively. Schomacker et al (151) reported spectra obtained in vivo at 337-nm excitation from 170 sites in the colon, and they used multivariate linear regression to differentiate hyperplastic and adenomatous polyps with 84% accuracy. They attributed fluorescence peaks at 460 nm to NADH fluorescence and those at

390 nm to collagen fluorescence, with an intervening valley at 425 nm due to hemoglobin reabsorption (152). Primary differences between the fluorescence of neoplastic and nonneoplastic tissues were due to collagen fluorescence and hemoglobin reabsorption; the authors suggest that since these changes reflect primarily morphological differences of polyps versus nonpolyps that the ability of laser-induced fluorescence to detect flat dysplasia will be limited (152). They noted dramatic differences between spectra obtained in vitro and in vivo; in particular, the contribution of NADH fluorescence decayed exponentially with time following excision with a half-life of approximately two hours (152). These changes call into question the relevance of in vitro results to clinical application (151).

High classification accuracy (97%) was also achieved in vivo by Cothren et al (153), who recorded spectra of 67 sites in the colon and were able to differentiate adenomas from normal mucosa and hyperplastic polyps based on (*a*) a drop in the maximum fluorescence intensity at 460 nm and (*b*) a relative increase in red fluorescence at 680 nm as tissue progressed from normal to hyperplastic to adenomatous. In a subsequent prospective in vivo study by Cothren (154) at 370-nm excitation, a similar algorithm could differentiate 172 sites as adenomatous or nonadenomatous with an 88% accuracy. Cothren (154) noted significant patient-to-patient variation in the fluorescence intensity of normal and adenomatous colon; in order to achieve 88% accuracy, he normalized all spectra to the peak intensity of each patient's normal mucosa. At UV excitation, Romer et al (155) showed that the fluorescence of normal colon is principally associated with collagen fibers in all layers of the bowel wall and with cytoplasmic granules within EOs present in the mucosa (155). In colonic adenomas, there were fewer collagen fibers within the mucosa and more fluorescent EO granules present than in normal colon (155). Bottiroli performed fluorescence microspectroscopy of normal and neoplastic colon at 366-nm excitation and observed similar fluorescent structures (156). Using confocal fluorescence microscopy, Fiarman et al (157) showed that at 488-nm excitation, the fluorescence of the normal colon mucosa is primarily associated with the lamina propria, while the mucosa of adenoma and hyperplastic polyps contain fluorescent epithelial cell cytoplasm, with decreased lamina propria fluorescence. Manoharan et al (158) have presented a tissue optics model that utilizes fluorescence line shapes and distributions of these structures to predict the 370-nm excited fluorescence spectra of colon tissue in vivo. The spectral differences between adenomas and normal mucosa were due to mucosal collagen fluorescence, dysplastic cell fluorescence, submucosa fluorescence, and hemoglobin attenuation. The model can be used to extract quantitative contributions of each of these parameters from tissue spectra (158). Based on the

model, Manoharan et al (158) predict that identification of flat dysplasia will
be possible using fluorescence spectroscopy.

Lohmann et al (159) investigated the utility of fluorescence emission spec-
troscopy for the recognition of cervical cancers and precancers in vitro. Using
365-nm excitation, they found that the fluorescence of normal and abnormal
cervix exhibited a single peak with an emission maximum at 475 nm. As tissue
progressed from normal to precancer, the fluorescence intensity increased, with
the degree of increase proportional to the degree of dysplasia (159). In contrast,
the fluorescence of tumors was very small, with a rise in intensity at the border
between malignant and healthy tissue (159). To determine the localization of
this naturally occurring fluorescence, Lohmann et al (159) investigated normal
and neoplastic cervices through the fluorescence microscope at 340- to 380-
nm excitation. The epithelium of both normal and neoplastic cervix exhibited
only a very weak fluorescence; the connective tissue adjacent to the epithelium
was much more highly fluorescent in sections from dysplastic cervices; and
regions of the cervix occupied by invasive cancer showed little fluorescence,
while the adjacent healthy tissue was highly fluorescent (159). Glassman et al
(160) measured fluorescence emission spectra of normal and cancerous gyne-
cological tissues in vitro at 300- and 320-nm excitation. Consistent differences
were seen in the fluorescence of malignant and nonmalignant tissues from all
sites; two intensity ratios were found useful for discrimination of malignant
samples (160). Glassman et al (161) have also reported fluorescence excitation
spectra of normal and neoplastic gynecological tissues obtained in vitro at 460-
nm emission. They attributed the fluorescence of gynecological tissues at this
emission wavelength to a combination of collagen, elastin, and NADH (161).
The differences observed in the fluorescence intensity ratio is consistent with
either an increase in NADH or collagen fluorescence or a decrease in elastin
fluorescence (161).

Richards-Kortum et al (162–168) have investigated the use of laser-induced
fluorescence spectroscopy for the diagnosis of cervical precancers [squamous
intraepithelial lesions (SILs)] in vivo. Their results demonstrate that a spec-
troscopically based algorithm can be developed to differentially diagnose SILs
in vivo, with a similar sensitivity and significantly improved specificity rela-
tive to current detection methods. Mahadevan et al (162) demonstrated that
the greatest differences in the emission spectra of nondiseased and diseased
cervical tissues in vitro occur at excitation wavelengths near 340, 380, and 460
nm. Fluorescence spectra were acquired in vivo from 114 cervical sites from
a group of 28 patients at 337-nm excitation (163, 164). A two-stage spectro-
scopic algorithm based on empirically determined spectral parameters could
differentiate between: (*a*) SILs and normal epithelia and (*b*) high-grade SILs

and low-grade SILs. Both stages of the algorithm performed with a similar sensitivity and significantly improved specificity relative to colposcopy (165).

The diagnostic contribution of spectra at multiple excitation wavelengths has been investigated by Ramanujam et al (166–168). Tissue spectra from 40 patients at 337- and 380-nm excitation and 24 patients at 337- and 460-nm excitation demonstrated that the diagnostic potential of spectra at these excitation wavelengths complements that at 337-nm excitation alone (167). This finding indicates that the tissue spectra at all three excitation wavelengths are necessary for the development of an optimal spectroscopic algorithm for the differential diagnosis in vivo of SILs.

Ramanujam et al (167) describe a method to develop diagnostic algorithms that overcome limitations of the empirically derived two-stage algorithm (163, 164). Preprocessing methods that do not require a priori information were utilized to calibrate for interpatient and intrapatient variation in tissue fluorescence spectra; principal component analysis (PCA) was used to dimensionally reduce each type of preprocessed spectral data with minimal information loss; finally, a probability-based classification algorithm was developed using logistic discrimination (166). In addition, component loadings calculated from PCA could be used to identify fluorescence intensities at the minimum number of emission wavelengths required for the diagnostic algorithm to perform so that there would be a minimum decrease in predictive ability relative to using the entire emission spectra (166).

Tissue spectra were acquired in vivo at all three excitation wavelengths (337, 380, and 460 nm) from 100 patients (168). Tissue spectra at multiple excitation wavelengths were analyzed to determine if the diagnostic performance of each constituent algorithm developed previously could be improved using tissue spectra at a combination of two or three excitation wavelengths rather than at a single excitation wavelength. In summary, fluorescence spectra at multiple excitation wavelengths can be used to develop composite diagnostic algorithms for the differential diagnosis of SILs and high-grade SILs with a similar sensitivity and significantly improved specificity relative to expert colposcopy (168). Furthermore, component loadings developed from principal component analysis were used to select fluorescence intensities at 15 pairs of excitation and emission wavelengths, which could be used to redevelop modified composite algorithms that perform with a minimum decrease in predictive ability (168).

Alfano et al measured the fluorescence emission spectra of normal and neoplastic breast tissue in vitro from two patients at 488 and 457.9 nm (169). Normal and malignant tissues both showed a principal peak at about 515 nm, while the spectrum of the normal sample also exhibited additional maxima at

556 and 592 nm (169). When the same samples were excited at 457.9 nm, the spectrum of normal breast exhibited intense sharp peaks, which were attributed to resonance Raman scattering at 1037, 1243, 1588, 2761, and 2963 cm^{-1} (169). In a subsequent in vitro study of the 15 normal breast samples, 11 showed Raman peaks at all excitation wavelengths investigated; those specimens with Raman peaks tended to have more fat and to appear yellow (170). A classification accuracy of 91% was achieved using these features (170). To determine whether differences in fluorescence could be attributed to differences in the normal and cancerous cells, Glassman et al (171) examined the fluorescence emission spectra at 353-nm excitation of normal and malignant breast cell lines (171). A peak observed at 450 nm was assigned to reduced pyridine nucleotide fluorescence, a shoulder at 525 nm was assigned to flavin fluorescence (171). The ratio of the intensity at 450 nm to that at 525 nm was greater than 2 for the malignant cell line and less than 2 for the normal cell line (171). However, Lohmann et al found that the fluorescence of breast tissue at 340- to 380-nm excitation was associated primarily with connective tissue fibers in between lactiferous ducts and lobular complexes (172). In the malignant tissues, the fluorescence of healthy adjacent connective tissues is even higher than that observed in normal breast (172).

Lohmann & Bodecker (173) found that fluorescence emission spectra at 365-nm excitation could be used to differentiate nevi from dysplastic nevi (precancerous) and malignant melanomas (cancerous) in an in vivo study of 147 patients . The ratio of the fluorescence intensity at 470 nm within and outside pigmented lesions was substantially higher for dysplastic nevi and melanomas than for nevi (173). Sterenborg et al (174) measured fluorescence excitation-emission matrices (EEMs) of normal skin and human skin tumors in vivo at excitation wavelengths ranging from 375 to 600 nm. In contrast to Lohmann & Bodecker, Sterenborg et al (174) found no correlations between either the shape of the fluorescence spectra or the spatial distribution of fluorescence intensity and the histopathology of the tissue measured. They concluded that autofluorescence diagnosis of skin tumors is not currently feasible (174). Zeng et al (175) has measured the distribution of autofluorescence in human skin at 442-nm excitation by using a fluorescence microspectrophotometer. A similar intensity distribution of fluorescence was observed by Lohmann & Paul (176) at 340- to 380-nm excitation. Zeng et al (177) described a spectrometer to measure the fluorescence and diffuse reflectance of skin in vivo. Based on in vivo studies, they concluded that the fluorescence spectrum of skin at 442 nm is modulated substantially by the scattering and absorption properties of skin tissue (177). Zeng et al have investigated the photobleaching of skin fluorescence in vivo with 442-nm excitation (178).

Roy et al (179) measured fluorescence EEMs in vitro of 20 normal, dysplastic (precancerous), and malignant (cancerous) squamous tissues from the oral cavity at 250-to 500-nm excitation. All abnormal samples showed enhanced fluorescence in the red region, with a prominent excitation emission maximum at 410-nm excitation, 635-nm emission; red tumor fluorescence has been attributed to porphyrins by other authors (180). Preliminary comparisons of the fluorescence spectra of normal and malignant tissue from the oral cavity have been conducted by Schantz and coworkers (181–183). They have shown that NMBA-induced esophageal premalignancy results in specific changes in tissue autofluorescence in a rat model (181). This group has also applied this technique to a multicellular tumor spheroid model and shown that treatment with retinoic acid results in changes in the fluorescence spectra that are consistent with a decrease in the peak associated with reduced nicotinamide-adenine dinucleotide and an increase in the peaks associated with flavins, tryptophan, and cytokeratins (182). This suggests that fluorescence can be used to monitor alterations in cellular electron transport and tryptophan-containing protein metabolism, which may be important in identifying premalignant lesions. Limited clinical trials have been conducted using a Xenon-based fluorescence spectrophotometer with a fiber probe to measure two fluorescence excitation (300- and 340-nm excitation) and two fluorescence emission spectra (380- and 450-nm emission) at five sites in the oral cavity in a series of 41 controls and on the lesion and contralateral normal site in 16 oral tongue cancer patients (183). Discrimination between normal and neoplastic sites could be achieved at 340-nm excitation (183). Kluftinger et al (184) investigated the fluorescence of neoplasms of the oral cavity by using an animal model. A pseudocolor image was formed from the ratio of red to green fluorescence; areas of carcinoma in situ showed the highest fluorescence ratio, while those of dysplasia were also elevated from that of normal tissue (184). Using this technique to direct biopsy, 32 biopsies were obtained, all of which contained hyperplasia, dysplasia, carcinoma in situ, or invasive cancer; 13 of these lesions showed no grossly visible lesion by eye (184).

D'Hallewin et al (185) have demonstrated that autofluorescence spectroscopy at 365-nm excitation can be used to discriminate normal bladder carcinoma in situ and transitional cell carcinoma in vivo with high accuracy (185). The discrimination is based on the decrease in fluorescence intensity as tissue progresses from carcinoma in situ (average decrease of 2.6 times) to transitional cell carcinoma (average decrease of 3.2 times) (185).

Hung et al (186) examined the bronchial fluorescence of 32 patients with severe dysplasia, carcinoma in situ, and invasive tumors at 405-, 442-, and 488-nm excitation in vivo (186). Spectra at 405- and 442-nm excitation were

similar, with two emission maxima at 520 and 595 nm. Spectra of normal and abnormal tissue showed similar line shapes at these excitation wavelengths, but the intensity decreased progressively as tissue went from normal to severe dysplasia to carcinsoma in situ to invasive cancer (186). The fluorescence spectra of normal larynx and laryngeal tumors are similar to those of normal bronchial wall and bronchial tumors at 442-nm excitation (187). Lohmann et al examined the fluorescence of normal lung and lung tumors under the fluorescence microscope at 365-nm excitation (188). As in the case of skin and cervix, the areas of the tumor did not exhibit appreciable fluorescence compared to normal tissue, whereas the areas surrounding the tumors showed substantially brighter fluorescence than normal tissue (188). Palcic et al (189) have described an endoscope-based system that provides simultaneous white light images of the bronchial wall and pseudo-color images based on the ratio of autofluorescence emitted in two wavelength bands with 442-nm excitation. The performance of the fluorescence bronchoscope imaging system was compared to that of conventional white light bronchoscopy in 53 patients and 41 normal volunteers (190). Although the sensitivity of each technique was similar (94%), the specificity of the fluorescence technique (73%) was substantially higher than that of conventional bronchoscopy (48%) (190).

Fluorescence emission spectra of normal and neoplastic brain were recorded in vitro at 308-nm excitation from 79 samples from 5 patients (191). Peaks at 352 and 363 nm were attributed to tryptophan fluorescence, a peak at 383 to a combination of collagen and elastin fluorescence, and a peak at 460 nm to NAD(P)H fluorescence (191). When spectra of normal white and grey matter were compared, spectra were similar except for a 25% increase in the emission at 453 nm in grey matter, which is consistent with the fact that grey matter contains more mitochondria than white matter (191). The fluorescence intensity of astrocytomas were relatively weak compared to normal brain; the contributions of peaks at 398 and 453 nm were increased by approximately a factor of two in astrocytoma (191). Using simple ratios of fluorescence intensities, good discrimination between normal tissue and tumors was obtained (191). Montan & Stromblad (192) examined 337-nm excited fluorescence of normal and neoplastic brain tissue in vivo during craniotomy operations and in vitro following tissue preservation by freezing or formaldehyde. Preservation by freezing significantly altered both the fluorescence lineshape and intensity, while formaldehyde fixation did not affect spectral shape but did alter intensities (192).

Fluorescence from Exogenous Probes: Steady State

The use of exogenous, optically active agents has been an area of considerable research interest in a wide range of diseases. Using the ratiometric probe *bis*-carboxyethyl carboxyfluorescein (BCECF) administered in mice and dual

wavelength measurements, Mordon et al (193) demonstrated noninvasive mapping of tumor pH with an image-intensified CCD camera system. Russell et al (194) were able to track the extracellular pH in conscious mice undergoing hypercapnia by using fiber optic coupling; they employed an in vitro calibration curve for the ratio of fluorescent intensities as a function of pH and applied it to the ratio of intensities obtained from reflectance skin measurements in conscious mice. The success of these probes depends upon the small Stokes' shifts across which tissue absorption and scattering spectra are featureless (195).

Most prominently studied exogenous probes for tissues involve the use of photodynamic agents and other fluorescent agents with absorption bands in the red or NIR region as tumor-localizing agents. The use of exogenous porphyrins to image and detect tumors on the basis of fluorescence has been suggested by several authors (for review, see 196). Hematoporphyrin derivative (HpD) and other purified versions such as Photofrin II (PPII) are of considerable interest as therapeutic agents in photodynamic therapy. Once injected, the monomeric forms of these drugs accumulate in tumor tissues. When excited to a triplet state by the absorption of light, cytotoxic singlet oxygen is generated through the energy transfer process to molecular oxygen (197). Recently, Tanielian & Heinrich (198) have shown that the formation of cytotoxic singlet oxygen results primarily from the monomeric fraction of HpD. Nilsson et al (199) evaluated the use of a carotenoporphryin in which the carotene moiety quenches the triplet states of the porphyrin compound and thereby renders it an ineffective photodynamic agent. Because the singlet state is preserved, the fluorescence from radiative relaxation makes it an excellent tumor localization substance without the side effects of cytotoxicity to skin and other organs. Other investigators have employed HpD (200), hematoporphyrin (Hp) (201), polyhematoporphyrin ester (PHE) (201, 202), sulphonated phthalocyanines (201–203), and benzo porphyrin derivative (BPD)-monoacid (202, 204) for tumor detection based upon reemitted fluorescence. Improved detection of arterial plaque in New Zealand white rabbits has also been reported by Ye and coworkers (205) following i.v. administration of β-carotene, an agent that preferentially binds to plaque and reduces the total fluorescence emission at 488-nm excitation. Another optically active, exogenous agent for diagnostic capabilities is indocyanine green (ICG), which has been used clinically for cardiac output measurements and liver assessment for over 30 years. The tricarbocyanine dye has an absorption band in the NIR region ($\sim$ 800 nm) and has peak fluorescence at 840 nm. Upon i.v. administration, the dye is tightly bound to serum albumin and partitioned in the vascular space, except in diseases whereby vascular integrity is compromised, such as in the case for burn victims (206) or as a result of tumor angiogenesis (207).

Although these applications seek to use exogenous fluorescence in tissue for localization of disease, it is often desirable to know the concentration of drug in the tissues in order to alter therapy and to predict its efficacy. For example, there has been a plethora of investigations seeking to noninvasively track the time-dependent pharmacokinetics of fluorescent agents (208–210). Generally, these studies depend upon developing an empirical correlation between detected fluorescent signals and bioassays in which tissues are harvested and analyzed for the fluorophore of interest. Approaches using an appropriate model of fluorescent and excitation light propagation to determine drug concentration have yet to be applied. However, recognizing that CW dual-wavelength measurement of the reemitted fluorescence signals from Hp are distorted by differences in optical properties at the excitation and emission wavelengths, Sinaasappel & Sterenborg (73) found that the concentration of Hp can be obtained from CW measurements in the presence and in the absence of the administered drugs, assuming that the concentration of drug is spatially uniform. Exogenous probes developed for microscopy also have in vivo applications. For example, the use of voltage-sensitive exogenous dyes has been demonstrated in vivo by using noninvasive optical techniques coupled with an implanted window on a monkey cortex (211).

Fluorescence Lifetimes

Measurement of fluorescence dynamics or fluorescence lifetime provides additional spectroscopic information regarding the tissue and cellular environment in which the fluorophore resides. The nonradiative decay from the triplet state is most often associated with photooxidative damage in biological systems, owing to the cytotoxic singlet molecular oxygen produced from the nonradiative relaxation from the excited triplet state. Since triplet states are long-lived (milliseconds), they are indicative of increased likelihood for photooxidative damage due to the increased probability for encounter with molecular oxygen (212). Singlet excited states are comparatively short-lived (picoseconds to nanoseconds) and are reflective of the binding or the environment of the fluorophore. Regardless, the measurement of lifetime(s) provides an alternative spectroscopic evaluation of the biological environment and photoactivity that is independent of the concentration of the fluorophore. Table 2 is a comprehensive listing of lifetimes of the endogenous and exogenous fluorophores reviewed in this section.

Measurement of lifetime has been primarily confined to nonscattering systems, using time-domain and frequency-domain approaches. In the time-domain approach, the time-dependent reemission intensity is monitored following an incident pulse of excitation light. The reemission light exponentially decays with $\sum \beta_i \exp(-t/\tau_i)$ in which i is summed over all excited states. The coefficient, β_i, represents the fraction of reemitted light attributable to the energy

level *i*. In the frequency-domain technique, the diluted fluorophores are activated by a steadily modulated source. The reemitted fluorescent light is both phase-shifted, θ, and amplitude modulated, *M,* relative to the incident excitation light. If only one activated state predominates, then the reemission light will be phase shifted by $\tan^{-1}(\omega\tau)$ and amplitude demodulated by $1/[1 + (\omega\tau)^2]^{1/2}$. The analysis of lifetimes due to multiple activated states is also possible (66). Microscopy applications of fluorescent lifetime imaging are sought by several groups who are using time (213–215), frequency (216), and confocal imaging (217).

Since the contribution of scatter is minimal in microscopy applications, lifetime determinations are accurate. However, in tissues, photon time-of-flights are significant because of scatter, thereby contributing to the kinetics of the fluorescence reemission and distorting lifetime measurements.

FLUOROPHORE LIFETIMES OF ENDOGENOUS SPECIES   Lifetime measurements of coenzymes NAD(P)H and flavins have been reported in solution and in microscopy applications. The reduced pyridine coenzymes exhibit biexponential decay kinetics with the predominant relaxation associated with a short-lived activated state ($\tau_1 = 0.45 - 0.60$ ns) accompanied by a longer-lived component ($\tau_2 = 1.4 - 2.2$ ns) (215). Oxidized flavomononucleotide (FMN) exhibits a single exponential decay with a lifetime of 5 ns but is reduced to picoseconds when bound (215). When free, NAD(P)H has a lifetime of 0.4 ns (218) but exhibits an increased lifetime of 1–3 ns when bound (215, 218). Schneckenburger & Konig (215) used video-enhanced time-domain single-photon counting to determine the NAD(P)H lifetime of normal and wild-type strains *Saccharaomyces cerevisiae* with genetic deficiencies in cytochromes a, aa$_3$, and b in the respiratory chain. Their results showed triexponential decays; the additional lifetime component was due possibly to the presence of bound and unbound forms as well as to the contribution of other coenzymes. The wild-type strains displayed a reduction in the short-lived fluorescent component at 500 nm, owing possibly to the increase in bound flavins.

The measurement of endogenous fluorescence lifetime has applications for diagnosis in tissues. For example, in normal and atherosclerotic arterial wall, Andersson-Engels et al (219) found that the fluorescence at 400 nm upon excitation at 320 nm displayed a triexponential decay with components of 0.3, 2, and 7 ns. Although the lifetime components remained constant from diseased to normal state, the contribution of the long-lived component to the total reemitted fluorescent signal increased with the atherosclerotic plaque. Feld and coworkers found similar lifetime components in normal arterial wall (220).

Tata et al (221) monitored fluorescence reemission from malignant and normal rat kidney tissues. Their results show longer decay times associated with

Table 2 Lifetimes of fluorescent and phosphorescent probes

Species	Solvent	Excitation/ emission (nm)	τ_1 (ns)	% Intensity	τ_2 (ns)	% Intensity	τ_3 (ns)	% Intensity	Reference
NAD(P)H[a]	Water	365/>410	0.45–0.60	(75–90)	1.4–2.2	(10–25)			282
	Water								66
NAD(P)H	Intact and defective yeast cells	365/450	0.2–0.3	30	1.4–2.4	40	6.0–8.0	30	282
Flavins	Intact yeast cells	365/500	0.2–0.35	45	2.0–3.0	25	6.0–8.0	30	282
Flavins[b]	Defective yeast cells	365/500	0.30–0.50	35	2.0–3.0	30	6.0–8.0	35	282
Oxidized flavomono- nucleotide	Water	436/500	5.2	100					282
FMN									
NAD(P)H[c]	Normal arterial wall	320/400	0.3		2		7		202
	Athlerosclerotic arterial wall	320/400							
Flavins	Normal rates kidney	488/(500–550)	.357 ± 0.018	0.27	1.220 ± 0.035	0.63			224
		488/(600–650)	.204 ± 0.011	0.47	1.0 ± 0.006	0.53			
	Cancerous rat kidney	488/(500–550)	.223 ± 0.015	0.59	1.966 ± 0.037	0.41			
		488/(600–650)	.236 ± 0.014	0.67	1.963 ± 0.037	0.33			
Collagen	Powder		2.7	25	8.9	35			223
Elastin	Powder		2	75	6.7	65			223
Zn-Protoporphyrin	DMSO	400/650–670	2	100					223
Protoporphryin IX	DMSO	650–670	17	89	3	11			223
Coprotoporphyrin IX	DMSO	650–670	20	100					223
Protoporphyrin photoproduct	DMSO	650–670	0.7	38	4.5	62			223

Table 2

Photofrin II[d]

0 mM CTAB (Cetyltrimethyl-ammonium bromide)	364/615	15.4	100			0.74	18.1	227
0 mM CTAB	364/630	14.6	64.3	2.97	17.6			
0 mM CTAB	364/675	14.36	81.3	1.95	18.7			
0.005 mM CTAB	364/615	15.04	94.3	2.44	5.7	0.42	62.9	
0.005 mM CTAB	364/630	14.44	22.4	2.37	14.7	0.67	48.5	
0.005 mM CTAB	364/675	14.07	20.3	2.21	31.2	0.58	12.5	
0.01 mM CTAB	364/615	14.99	80.7	2.27	6.8	0.5	75.4	
0.01 mM CTAB	364/630	14.15	10.4	2.2	14.2	0.83	67.4	
0.01 mM CTAB	364/675	13.84	7.3	2.43	25.3	0.67	53.2	
0.05 mM CTAB	364/615	13.88	18.2	2.47	28.5	0.62	78	
0.05 mM CTAB	364/630	12.41	3.1	2.66	18.9	1.06	62.7	
0.05 mM CTAB	364/675	8.17	3.2	2.67	34.1	0.96	35.3	
0.1 mM CTAB	364/630	10.5	21.5	3.71	43.2			
0.1mM CTAB	364/675	7.55	49.2	3.61	50.8			
1 mM CTAB	364/630	16.05	89.6	3.38	10.4			
1 mM CTAB	364/675	15.28	63.1	5.75	36.9			
In L1210 mouse cells, 4 hr following i.p. admin.	364/630	14.9	40.9	4.91	18.32	1.18	41.58	224
In L1210 mouse cells, 12 hr following i.v. admin.	364/630	14.81	7.3	4.65	25.49	1.08	67.27	224

(cotinued)

Table 2 (continued)

Species	Solvent	Excitation/ emission (nm)	τ_1 (ns)	% Intensity	τ_2 (ns)	% Intensity	τ_3 (ns)	% Intensity	Reference
Hematoporphryin	In L1210 mouse cells, 4 hr following i.p. admin.	364/630	15.3	45.39	4.32	18.16	1.11	36.46	
HPD	In L1210 mouse cells, 12 hr following i.v. admin.	364/630	14.36	10.83	3.12	20.07	0.61	69.1	219
HPD	Tumor tissue in DHE-injected rat	320/630	0.7		6		17	(Higher)	
	Normal tissue in surrounding muscle	320/630					17	(Lower)	
ALA-induced PP	In vivo tumor flank								232
	Before irradiation	?	230 ps	17	17.1	83			
	After irradiation	?	270 ps	5.5	5	45			
Protoporphryin	Incubated meercat kidney cells	420/610–690	1–2		2.0–3.0		11.0–14.0		230
	Dorsal skinfold of hamster PBS solution								
Aluminum phthalocyanine	In L1210 mouse cells, 4 hr following i.p. admin.	364/630	5.18	86.33	1.52	13.67			224
Aluminum phthalocyanine	In L1210 mouse cells, 12 hr following i.v. admin.	364/630	5.9	39.74	2.87	50.24	0.93	10.01	
Aluminum phthalocyanine	PBS	610/>645	5.0 ± 0.1						
	PBS + BSA		5.5 ± 0.2	92.0 ± 1	1.0 ± 0.2	8 ± 1			229
	0.01 mM CTAB + 0.1 M PBS		6.0 ± 0.1						
	1% Triton in 0.1 M PBS		5.9 ± 0.1						
	Cultured leukemic cells		2.2 ± 0.4	~50	6.1 ± 0.2	~50			
	Human erythroleukaemic cells								
3-Hydroxy kynuremine	Extracts of human eye (young)	355/>355	24 μs		400 μs				222
	Extracts of human eye (old)		31–61 ps						

a Deficient cell fluorescence is four times higher.
b T_1 is lower but represents more fluorescence in intact cells.
c Calcified plaques have a higher ratio of slow (400 nm) to fast fluorescence (480 nm).
d Cationic micelles influence aggregation.

flavin molecules as a result of a smaller number of nonradiative pathways by which energy can be transferred from the bound flavins. Since fluorescence reemission is distorted by tissue scatter, in addition to fluorophore lifetime, lifetime constants may also reflect differences in tissue scatter with disease.

Another group of investigators monitored fluorescent decay kinetics from the lens protein that is presumably responsible for photooxidative protection. This lens protein, 3-hydroxy kynurenine, reduces the photooxidative stress from ambient radiation by absorbing light in the 300–400 nm region to form an excited singlet state with a picosecond decay time (222). For aged lens, the absorption results in long-lived excited states (millisecond) that increases the potential of photooxidative damage and age-related changes in the human lens.

FLUORESCENCE LIFETIMES OF EXOGENOUS PROBES   Many reports have discussed the use of exogenous porphyrins to image and detect tumors on the basis of fluorescence lifetime. Because the decay kinetics of porphyrins show a long-lived component (>10–15 ns) over endogenous fluorophores (< 1–3 ns), investigators have sought an appropriate window to isolate diseased tissues by using gated, intensified CCD video cameras (223–225) to image the fluorescence reemitted from tissues following porphyrin administration. In addition to detecting tumors by using time-gating procedures with exogenously induced porphyrins, Konig et al (223) provided images to detect dental caries and plaque from the long-lived fluorescence due to endogenous protoporphyrin IX (PpIX) produced by bacteria.

Various components of exogenous photosensitizers partition differently in different tissue types (226). Porphyrins exhibit multiple lifetimes depending upon the states of the porphyrin molecule: Aggregated species exhibit a fast fluorescence decay with lifetime between 0.1 and 0.2 ns; dimers have a fluorescent lifetime of 1.5–3 ns, while monomers have fluorescent lifetimes on the order of 10–14 ns. Once injected into the body, the drug deaggregates (presumably resulting from the hydrophobic environments) into the therapeutic monomeric form as tracked from lifetime measurements. Although it is the triplet states of the monomeric fraction that are attributed to photodynamic action, the fluorescence from the singlet state provides information on the local environment. From fluorescence lifetime measurements of leukemia cells harvested from mice, Cubeddu et al (224) have shown that i.v. administration results in a more efficacious disaggregation to form monomer from HpD and PPII than does intraperitoneal injection. These results are indicated by the reduction of short-lived fluorescence component with i.v. administration. Compartmentalization in hydrophobic membranes may mediate the disaggregation process, as indicated from the results for HpD by Cubeddu et al (227) and for zinc phthalocyanines (another photodynamic agent) by Valduga et al (228). They

found that in cationic micelles or unilamellar vesicles, the photodynamic agent is completely dissociated into its monomeric form, which indicates that partitioning in hydrophobic environments mediates efficacy of the therapy. Because hydrophobic agents have a greater partition in neoplastic cell membranes than normal membranes, these results point to the increased uptake of monomeric drug into tumors. Lifetime measurements of phthalocyanines in leukemia cells show a monoexponential decay of approximately 5 ns (224) as well as in aqueous and hydrophobic environments, indicating the lack of aggregation (224, 229). However, Ambroz et al (229) found biexponential decays indicating subcellular compartmentalization of the compound into different environments. Indeed, several investigators have monitored the monomeric fraction of drug from the fluorescent decay of porphyrins in cell compartments by using time-domain fluorescence lifetime microscopy (224, 226, 230).

An alternative to administering endogenous porphyrins is to induce cells to generate their own photosensitizer through the administration of 5-aminolaevulinic acid (ALA), which is converted into PpIX. In the case of ALA-induced PpIX in cells, a long-lived monoexponential decay was found, indicating that the porphyrin existed in its monomeric form (231). Using Rhodamine 123 as a selective mitochondrial marker, Seidlitz et al (226) showed that its intracellular distribution mimicked that of monomeric porphyrins, indicating that the efficacious component was indeed compartmentalized in the mitochondria. Measurement of reemitted fluorescence from ALA-incubated skin reflected complicated decay kinetics, owing to the contribution of scatter in the measurements. Nonetheless, the long-lived component of the fluorescence due to the ALA-stimulated PP monomers provided substantially more fluorescence over autofluorescence 10 ns after excitation, providing a diagnostic window for detection of the disease (215).

Following irradiation of ALA-induced PP, Koenig et al (232) observed a shortening of the decay times, due presumably to the production of short-lived photoproducts, which involves the formation of singlet oxygen in their conversion. Ambroz et al also found that the short-lived component of AlS_2Pc disappeared upon irradiation, owing to the oxidation of subcellular sites (229). Despite their differences, these studies suggest that the measurement of porphyrin lifetimes during photodynamic therapy may provide information on singlet oxygen formation and efficacy of treatment. Recently, Hutchinson et al (71, 74) found that the lifetime and yield of the fluorophore can be determined from frequency-domain measurement of reemitted excitation and fluorescent light independently of tissue scattering from measurement of phase-shift and amplitude modulation of the reemitted excitation and emission light. Other photodynamic agents, such as bacteriochlorin, a derivative of bacteriochlorphyll, has an absorption band at 760 nm, a wavelength where tissue penetration is maximal and

laser diodes are available for therapeutics and diagnostic measurements (233). Other photosensitive agents with absorption bands and fluorescent yields in the red are the chlorins, purpurins, and cyanine dyes.

Another application of lifetime-sensitive exogenous agents involves the non-invasive measure of oxygen tension from the phosphorescence quench of palladium (Pd)-coporphyrin compounds (234). Although photodynamic action depends upon the quenching of the excited triplet state to produce cytotoxic oxygen, the reduction in the phosphorescent lifetime can also be used to determine the oxygen concentration. Quenching of phosphorescent probes is limited by the probability for collision between the excited triplet state and oxygen. Therefore, as the concentration of molecular oxygen increases and the probability for collisional encounter with porphyrin increases, the decay of phosphorescence (or lifetime) decreases. Since decay times are on the order of 100 μs to 10 ms, simple flashlamp technology and video camera detection can be used to detect phosphorescence decay kinetics and to determine the local oxygen concentration via the Stern-Volmer relationship (234, 235). Applications to date include perfused tissues (236), cat brain cortex (237), interstitial tumor tissue in the dorsal skin chamber (238), and in vivo subcutaneous tumors (58). Because porphyrins with red excitation and emission spectra are now common, the capacity to detect phosphorescence, which originates deep within tissues, offers the capability to noninvasively monitor oxygenation deep within tissues. Recently, Sevick-Muraca & Burch (70) used computational arguments suggesting that the origin of the predominant phosphorescent signals detected at the tissue surface and elicited from surface excitation will come primarily from subsurface tissues. These computational findings require experimental confirmation.

Finally, the development of exogenous dyes with lifetime sensitive to a variety of analytes promises new opportunities for biodiagnostics monitoring (207). The development of multiplex dyes, which are excited and detected at similar wavelengths but are partitioned and differentiated on the basis of the lifetimes because of small structural changes of side groups (239, 240), offers enormous opportunities if these dyes can be synthesized for short-term stability and nontoxicity.

Raman Spectroscopy for Tissue Diagnosis

Most in vivo spectroscopy studies have concentrated on elastic scattering and fluorescence spectroscopies, since these signals can be obtained quickly with a good signal-to-noise ratio. However, Raman spectroscopy, an inelastic scattering process, provides a wealth of spectrally narrow features that can be related to the specific molecular structure of the sample. Because of these advantages, Raman spectroscopy has been used to study static and dynamic properties of biologically important molecules in solution, in single living cells, in cell cultures, and more recently, in tissues (for example, see 241–243).

The positions and relative intensities of various Raman spectral bands can be used to probe primary, secondary, tertiary, and quaternary structures of large biological molecules. The fingerprint spectral region, from approximately 700–1900 cm^{-1}, contains a series of sharp bands that can be used to characterize a particular molecule and, in some cases, to identify the composition of complex, multicomponent samples. Based on the success of Raman spectroscopy in biology, many groups have recognized its potential in the study and diagnosis of disease. However, early attempts to measure Raman spectra of cells and tissues were hindered by two factors: (*a*) the highly fluorescent nature of these samples and (*b*) instrument limitations, which necessitated long integration times and high-power densities to achieve spectra with good signal-to-noise ratios. Improvements in instrumentation in the last decade, particularly in the NIR region of the spectrum, where fluorescence is reduced, have engendered a dramatic increase in biomedical applications of Raman spectroscopy. Several articles have reviewed this field (244–246) and illustrated the diversity of potential applications, ranging from monitoring cataract formation in vivo (244) to the precise molecular diagnosis of atherosclerotic lesions in coronary arteries (247). Most recently, reports have begun to appear that suggest that Raman spectroscopy has the potential to diagnose and study the evolution of precancerous and cancerous lesions in human tissues in vivo (248–251).

Raman spectra have been measured and used to analyze changes in the structure and environment of many of the molecules that participate in neoplastic transformation. Raman can be used to probe protein structure at several different levels (for example, see 241–243, 252). The use of Raman spectroscopy for the analysis of DNA conformation has recently been reviewed (253). In general, bands in the Raman spectrum of DNA can be assigned to vibrations of either the sugar phosphate backbone or one of the four bases (253–260).

The initial Raman spectra of tissue were measured with visible laser excitation, using primarily the argon laser lines (for example, see 261, 262). Fourier transform (FT) Raman spectroscopy was used to measure tissue Raman spectra, typically using 1064 nm (Nd:YAG) for excitation with germanium detectors (245, 246). FT-IR Raman spectroscopy uses preresonance excitation to reduce the fluorescence contribution and thus allows the measurement of Raman spectra, even from highly fluorescent samples with little or no fluorescence (245). This technique yielded acceptable signal-to-noise ratios with moderately high-power densities, but collection times on the order of 30 min were required to obtain spectra of highly fluorescent scattering tissues such as human artery (263). More recently, the development of diode lasers and cooled silicon CCD cameras sensitive in the NIR has enabled the measurement of tissue Raman spectra with NIR excitation. Diode lasers can provide excitation typically in the region of 750–850 nm, which allows the use of silicon detectors (sensitive

only to 1100 nm). The advantage of this technique is that fluorescence emission is reduced, and spectra with acceptable signal-to-noise ratios can be achieved with relatively short integration times (< 1 min) (264). Several experimental as well as mathematical tools have been proposed to separate the contribution of fluorescence to yield the intrinsic Raman scattering (263, 265–269).

Although many groups have suggested that Raman spectra could be useful for in vivo tissue analysis, instrument limitations described above have forced most studies to be conducted in vitro to assess the feasibility of clinical application. To biologically simulate in vivo conditions, most studies have been conducted with extracted tissues that have been frozen (with liquid nitrogen or dry ice) at the time of collection and thawed for study or fixed in formalin to prevent deterioration. Several groups have studied the effect of fixation on tissue Raman spectra obtained in vitro (270–272). These studies indicate that although some differences are observed in the Raman spectra of fresh and fixed tissues, the variation appears to be small and does not affect the potential diagnostic capability of the spectrum. This is in contrast to fluorescence spectroscopy, where fixation can induce significant changes in the tissue fluorescence spectrum (273). Another approach to address the difficulty of recording Raman spectra from human tissue in vivo is to use animal tissues. However, Raman spectra of animal tissues can in some cases differ from that of human tissues, resulting in conclusions not valid for humans (274, 275).

Raman spectroscopy has thus far been applied to cancer detection of epithelial and mesenchymal origin such as the breast (170, 248–250, 271, 277, 278), brain (272, 279), colon (249, 276), bladder (249), and gynecological tissues (248). In addition, precancer of the cervix has been investigated with Raman spectroscopy (251, 265); results suggest that in normal cervix, inflammation and metaplasia samples can be separated from precancerous samples, obviating a potential limitation of fluorescence spectroscopy–based algorithms. The ratio of intensities at 1655 to 1450 cm^{-1} has been consistently used to differentiate normal and cancerous tissues at different sites, including the brain, breast, and gynecological tissues. In several tissues, the second amide band at 1260 cm^{-1} contributes to differentiation as well. The potential to derive more detailed biochemical information exists but will require more complex microscopic and chemical studies.

CONCLUSIONS AND PERSPECTIVES FOR THE FUTURE

This review illustrates the diverse and promising potential clinical applications of quantitative biomedical optical spectroscopy. Elastic scattering, fluorescence, phosphorescence, and Raman spectroscopies contain a wealth of

information about the biochemical and morphological composition of tissue
that can, in principle, provide information about the presence and stage of dis-
ease in tissue. Limited clinical trials of these technologies have demonstrated
their abilities to detect atherosclerosis and neoplasia and to measure the concen-
tration of both endogenous and exogenous probes in order to gain information
about the physiological and pathophysiological state of tissue. However, nu-
merous groups have shown that extracting biochemical information from such
spectra is complicated by the interaction between tissue scattering and various
types of emission.

We believe that wide-scale clinical application of these techniques requires
research in three important areas. First, a better understanding of the interaction
between scattering and emission is needed, and novel algorithms to decouple
scattering and emission contributions are required to maximize the information
that can be obtained from biomedical spectra. Secondly, the connection between
tissue scattering and emission properties and tissue microstructure must be
understood in greater detail in order to predict which clinical conditions will be
best detected with optical methodologies and which conditions will potentially
lead to false positive and false negative diagnoses with optical methods. Finally,
moderate- and large-scale multicenter clinical trials of promising technologies
are needed in order to rigorously document their performance and compare
them to the current standard of care.

Literature Cited

1. Burghardt E. 1984. *Colposcopy Cervical Pathology Textbook and Atlas.* Stuttgart: Georg Thieme Verlag
2. American Cancer Society. 1995. Cancer Facts & Figures
3. Wilson BC, Jacques SL. 1990. *IEEE J. Quantum Electron.* 26(12):2186–99
4. Jobsis FF, Keizer JH, LaManna JC, Rosenthal M. 1977. *Appl. Physiol: Respirat. Environ. Exercise Physiol.* 43(5):858–72
5. Cope M, Delpy DT. 1988. *Med. Biol. Eng.*

Comp. 26(3):289–94

6. Hazeki O, Tamura M. 1989. *Adv. Exp. Med. Biol.* 248:63–69

7. Pisantadosi CA. 1993. *Methods Toxicol.* 2:107–26

8. Lemberg R, Legg JW. 1949. *Hematin Compounds and Bile Pigments.* New York: Interscience

9. DeBlasi RA, Quaglia E, Ferrari M. 1991. *Biochem. Int.* 25:24l–84

10. DeBlasi RA, Fantini S, Franceschini MA, Ferrari M, Gratton E. 1995. *Med. Biol. Eng. Comput.* 33:228–30

11. Matcher SJ, Elwell CE, Cooper CE, Cope M, Delpy DT. 1995. *Anal. Biochem.* 227:54–68

12. Takatani S, Ling J, 1994. *IEEE Eng. Med. Biol.* 347–57

13. Hazen KH, Arnold MA, Small GW. 1994. *Appl. Spectrosc.* 48(4):477–83

14. Patterson MS, Wilson BC, Feather JW, Burns DM, Pushka W. 1987. *Biochem. Photobiol.* 46(3):337–43

15. Van de Hulst HC. 1957. *Light Scattering by Small Particles.* New York: Wiley

16. Bohren CF, Huffman DR. 1983. *Absorption and Scattering of Light by Small Particles.* New York: Wiley

17. Cross DA, Latimer P. 1972. *Appl. Opt.* 11:1225–28

18. Sloot PMA, Hoekstra AG, Figdor CG. 1988. *Cytometry* 9:636–41

19. Steinke JM, Shepherd AP. 1988. *Appl. Opt.* 27:4027–33

20. Kessler FM, Appelbaum K, Albrecht HP, Mauch ED. 1989. *Phys. Med. Biol.* 34:1901–16

21. Saidi IS, Jacques SL, Tittel FK. 1995. *Appl. Opt.* 34:7410–18

22. Arnfield MR, Tulip J, McPhee MS. 1988. *IEEE Trans. Biomed. Eng.* 35:372–81

23. Jacques SL. 1989. *IEEE Trans. Biomed. Eng.* 36:1155–61

24. Beauvoit B, Kitai T, Chance B. 1994. *Biophys. J.* 67:2501–10

25. Troy TL, Page DL, Sevick-Muraca EM. 1996. *J. Biomed. Opt.* In press

26. Chance B, Liu H, Kitai T, Zhang Y. 1995. *Anal. Biochem.* 227:351–62

27. Liu H, Miwa M, Beauvoit B, Wang NG, Chance B. 1993. *Anal. Biochem.* 213:378–85

28. Maier JS, Walker SA, Fantini S, Franceschini MA, Gratton. 1994. *Opt. Lett.* 19:2062–64

29. Thomsen SL, Jacques SL, Flock ST. 1990. In *Laser-Tissue Interactions,* ed. SL Jacques, *Proc. Soc. Photo. Opt. Instrum. Eng.* 1202:2–10

30. Bosman S. 1993. *Appl. Opt.* 32:461–63

31. Zijp JR, ten Bosch JJ. 1993. *Appl. Opts.* 32:411–15

32. Brinkman J, ten Bosch JJ, Borsboom PCF. 1988. *Caries Res.* 22:257–62

33. Mourant JR, Bigio IR, Boyer J, Conn RL, Johnson T, Shimada T. 1995. *Lasers Surg. Med.* 17(4):350–57

34. Wilson BC, Patterson MS. 1986. *Phys. Med. Biol.* 31:327–60

35. Chandrasekhar S. 1950. *Radiative Transfer.* London: Oxford Univ. Press

36. Ishimaru A. 1987. *Wave Propagation and Scattering in Random Media.* New York: Academic

37. Duderstadt JJ, Hamilton LJ. 1976. *Nuclear Reactor Analysis,* pp. 103–44. New York: Wiley

38. Prahl S, van Gemert MJC, Welch AJ. 1993. *Appl. Opt.* 32:559–68

39. Kubelka P. 1948. *J. Opt. Soc. Am.* 38:448–57

40. Wilson BC, Adam G. 1983. *Med. Phys.* 10(6):824–30

41. Eddowes MH, Mills TN, Delpy DT. 1995. *Appl. Opt.* 34(13):2261–67

42. Patterson MS, Chance B, Wilson BC. 1989. *Appl. Opt.* 28:2331–36

43. Groenhuis RAJ, ten Bosch JJ, Ferwerda HA. 1983. *Appl. Opt.* 22:2456–62

44. Groenhuis RAJ, ten Bosch JJ, Ferwerda HA. 1983. *Appl. Opt.* 22:2463–67

45. Farrell TJ, Patterson MS, Wilson BC. 1992. *Med. Phys.* 19:879–88

46. Delpy DT, Cope M, van der Zee P, Arridge S, Wray S, Wyatt J. 1988. *Phys. Med. Biol.* 33(12):1433–42

47. O'Connor DV, Phillips D. 1984. *Time-Correlated Single Photon Counting.* London: Academic

48. Sevick EM, Chance B, Leigh J, Nioka S, Maris M. 1991. *Anal. Biochem.* 195:330–51

49. van der Zee P, Arridge SR, Cope M, Delpy DT. 1990. *Adv. Exp. Med. Biol.* 277:79–84

50. Chance B, Nioka S, Kent J, McCully K, Fountain M, Greenfield R, Holtom G. 1988. *Anal. Biochem.* 174:698–707

51. Ferrari M, Wei Q, Carraresi L, DeBlasi RA, Zaccanti G. 1992. *J. Photochem. Photobiol.* 16:141–53

52. Wyatt JS, Cope M, Delpy DT, van der Zee P, Arridge S, et al. 1990. *Dev. Neurosci.* 12:140–44

53. Cubeddu R, Canti G, Musolino M, Pifferi A, Taroni P, Valentini G. 1994. *Photochem. Photobiol.* 60:582–85

54. Vitkin IA, Wilson BC, Kaplan RS, Anderson RR. 1992. *J. Photochem. Photobiol. B* 16:235–39

55. Tromberg BJ, Svaasand LO, Tsay TT, Haskell RC. 1993. *Appl. Opt.* 32(4):607–16

56. Fishkin JB, So PTC, Cerussi AE, Fantini S, Franchesini MA, Gratton E. 1995. *Appl. Opt.* 34(7):1143–55

57. Patterson MS, Moulton JD, Wilson BC, Berndt KW, Lakowicz J. 1991. *Appl. Opt.* 30:4474–76

58. Wilson BC, Sevick EM, Patterson MS, Chance B. 1992. *Proc. IEEE* 80:918–30

59. Thompson RB, Frisoli JK, Lakowicz JR. 1992. *Anal. Chem.* 64:2075–78

60. Madsen SJ, Anderson ER, Haskell RC, Tromberg BJ. 1994. *Opt. Lett.* 19(23):1934–36

61. Cheong WF, Prahl SA, Welch AJ. 1990. *IEEE J. Quantum Electron.* 26(12):2166–85

62. Pickering JW, Prahl SA, van Wieringen N, Beek JF, Sterenborg HJCM, van Gemert MJC. 1993. *Appl. Opt.* 32:399–410

63. Ishimaru A. 1978. *J. Opt. Soc. Am.* 68:1045–50

64. Torres JH, Welch AJ, Cilesiz I, Motamedi M. 1994. *Lasers Surg. Med.* 14:249–57

65. Nilsson AMK, Berg R, Andersson-Engels S. 1995. *Appl. Opt.* 34(21):4609–19

66. Lakowicz JR. 1985. *Principles of Fluorescence Spectroscopy.* New York: Plenum

67. Richards-Kortum R, Rava RP, Cothren R, Mehta A, Fitzmaurice M, et al. 1989. *Spectrochimica Acta* 45A:87–93

68. Richards-Kortum R, Rava RP, Fitzmaurice M, Tong LL, Ratliff NB, et al. 1989. *IEEE Trans. Biomed. Eng.* 36:1222–32

69. Patterson MS, Pogue BW. 1994. *Appl. Opt.* 33:1963–74

70. Sevick-Muraca EM, Burch CL. 1994. *Opt. Lett.* 19:1928–30

71. Hutchinson CL, Lakowicz JR, Sevick-Muraca EM. 1995. *Biophys. J.* 68:1574–82

72. Bolin FP, Preuss LE, Taylor RC, Ference RJ. 1989. *Appl. Opt.* 28(12):2297–303

73. Sinaasappel M, Sterenborg HJCM. 1993. *Appl. Opt.* 32:542–48

74. Hutchinson CL, Troy TL, Sevick-Muraca EM. 1996. *Appl. Opt.* 35:2325–32

75. Keijzer M, Richards-Kortum R, Jacques S, Feld MS. 1989. *Appl. Opt.,* 28:4286–92

76. Stryer L. 1988. *Biochemistry.* New York: Freeman. 34th ed.

77. Avi-Dor Y, Olson JM, Doherty D, Kaplan NO. 1962. *J. Biol. Chem.* 237:2377–82

78. Chance B, Thorell B. 1959. *J. Biol. Chem.* 234:3044–50

79. Davis RP, Canessa-Fischer M. 1965. *Anal. Biochem.* 10:325–43

80. Chance B, Baltscheffsky H. 1958. *J. Biol. Chem.* 233:736–39

81. Masters BR, Chance B. 1993. In *Fluorescent and Luminescent Probes for Biological Activity,* ed. WT Mason, pp. 44–56. London: Academic

82. Campbell ID, Dwek RA. 1984. *Biological Spectroscopy.* Menlo Park, CA: Benjamin Cummings

83. Fujimoto D. 1977. *Biochem. Biophys. Res. Commun.* 76:1124–29

84. Blomfield J, Farrar JF. 1969. *Cardiovasc. Res.* 3:161–70

85. Thornhill DP. 1975. *Biochem. J.* 147:215–19

86. Eyre D, Paz M. 1984. *Annu. Rev. Biochem.* 53:717–48

87. Deyl Z, Macek K, Adam M, VanCikova O. 1980. *Biochim. Biophys. Acta* 625:248–54

88. Richards-Kortum R, Rava RP, Baraga J, Fitzmaurice M, Kramer J, Feld M. 1990. In *Optronic Techniques in Diagnostic and Therapeutic Medicine,* ed. R Pratesi. New York: Plenum

89. Poulsom R, Pignatelli M, Stetler-Stevenson WG, Liotta LA, Wright PA, et al. 1992. *Am. J. Pathol.* 141:389–96

90. Campo E, Perez M, Charonis AA. 1992. *Mod. Pathol.* 5(5):540–46

91. Wilson RG, Davis RE. 1983. *Adv. Clin. Chem.* 23:1–68

92. Merrill AH Jr, Henderson JM. 1987. *Annu. Rev. Nutr.* 7:137–56

93. Ink SL, Henderson LM. 1984. *Annu. Rev. Nutr.* 4:455–70

94. Bridges JW, Davies DS, Williams RT. 1966. *Biochem. J.* 98:451–68

95. Shimasaki H, Ueta N, Privett OS. 1980. *Lipids* 15:236–41

96. Collins VP, Thaw HH. 1983. *Mech. Aging Dev.* 23:199–214

97. Tsuchida M, Miura T, Aibara K. 1987. *Chem. Phys. Lipids* 44:297–25

98. Ball RY, Carpenter KLH, Mitchinson MJ. 1987. *Arch. Pathol. Lab. Med.* 111:134–39

99. Mitchinson MJ, Hothersall DC, Brooks PN, De Burbure C. 1985. *J. Pathol.* 145:177–83

100. Eldred GE, Miller GV, Stark WS, Feeney-Burns L. 1982. *Science* 16:757–59

101. Stark WS, Miller GV, Itoku KA. 1984. *Enzymology* 105:342–47

102. Sohal RS. 1984. *Enzymology* 105:484–87

103. Chio KS, Reiss U, Fletcher B, Tappel AL. 1969. *Science* 166:1535–36

104. Dillard CJ, Tappel AL. 1984. *Methods Enzymol.* 105:337–41

105. Weller PF. 1991. *N. Engl. J. Med.* 324:1110–18

106. Gleich GJ, Adolphson CR. 1986. *Adv. Immunol.* 39:177–253

107. Barnes D, Aggarwal S, Thomsen S, Fitzmaurice M, Richards-Kortum R. 1993. *Photochem. Photobiol.* 58:297–303

108. Mayeno AN, Hamann KJ, Gleich GJ. 1992. *J. Leukocyte Biol.* 51:172–75

109. Weil GJ, Chused TM. 1981. *Blood* 57:1099–104

110. Samoszuk MK, Espinoza FP. 1987. *Blood* 70:597–99

111. Garvie WHH. 1965. *Nature* 4978:1333–34

112. Policard A. 1924. *Compte-rendus Soc. Biol.* 91:1423–24

113. Ronchese F, Walker BS, Young RM. 1954. *Arch. Derm. Syph.* 69:31

114. Ghadially FN. 1960. *J. Pathol. Bact.* 80:345–51

115. Ghadially FN, Neish WJP. 1960. *Nature* 169:1124

116. Sharvill D. 1955. *Trans St. Johns Hosp. Derm. Soc.* 34:32

117. Ghadially FN, Neish WJP, Dawkins HC. 1963. *J. Pathol. Bact.* 85:77–92

118. Papazoglou TG. 1995. *J. Photochem. Photobiol. B* 28:3–11

119. Nishioka NS. 1994. *Exp. Invest. Endosc.* 4:313–26

120. Edholm P, Jacobson B. 1965. *J. Atheroscler. Res.* 5:592–95

121. Kittrell C, Willett RL, de los Santos-Pacheco R, Ratliff NB, Kramer JR, et al. 1985. *Appl. Opt.* 24:2280–81

122. Bergeron A, Douville Y, Duplain G. 1988. *Can. J. Phys.* 66:1035–39

123. Bosshart F, Utzinger U, Hess OM, Wyser J, Mueller A, et al. 1992. *Cardiovasc. Res.* 26:620–25

124. Leon MB, Lu DY, Prevosti LG, Macy WW, Smith PD, et al. 1988. *J. Am. Coll. Cardiol.* 12:94–102

125. Clarke RH, Isner JM, Gauthier T, Nakagawa K, Cerio F, et al. 1988. *Lasers Surg. Med.* 8:45–59

126. Baraga J, Rava RP, Taroni P, Kittrell C, Fitzmaurice M, Feld MS. 1990. *Lasers Surg. Med.* 10:245–61

127. Fitzmaurice M, Bordagaray J, Engelmann G, Richards-Kortum R, Kolubayev T, et al. 1989. *Am. Heart J.* 118:1028–38

128. Verbunt RJAM, Fitzmaurice MA, Kramer JR, Ratliff NB, Kittrell C, et al. 1992. *Am. Heart J.* 123:208–16

129. Gmitro AF, Cutruzzola FW, Stetz ML, Deckelbaum LI. 1988. *Appl. Opt.* 27:1844–49

130. Oraevsky AA, Jacques SL, Pettit GH, Sauerbrey RA, Tittel FK, et al. 1993. *Circ. Res.* 72:84–90

131. Gaffney EJ, Clarke RH, Lucas AR, Isner JM. 1989. *Lasers Surg. Med* 9:215–28

132. Laifer LI, O'Brien KM, Stetz ML, Gindi GR, Garrand TJ, Deckelbaum LI. 1989. *Circulation* 80:1893–901

133. Gindi GR, Darken CJ, O'Brien KM, Stetz ML, Deckelbaum LI. 1991. *IEEE Trans. Biomed. Eng.* 38:246–52

134. Deckelbaum LI, Sarembock IJ, Stetz ML, O'Brien KM, Cutruzzolla FW, et al. 1988. *Opt. Fibers Med. III, SPIE* 906:314–19

135. Deckelbaum LI, Lam JK, Cabin HS, Clubb KS, Long MB. 1987. *Lasers Surg. Med.* 7:330–35

136. Blankenhorn DH, Braunstein H. 1958. *J. Clin. Invest.* 37:160–65

137. Sartori MP, Sauerbrey R, Kubodera S, Tittel FK, Roberts R, Henry PD. 1987. *IEEE J. Quantum Electron.* 23:1794–97

138. Richards-Kortum R. 1987. *Understanding laser-induced fluorescence spectra of human artery wall with applications to diagnosis of atherosclerosis.* MS thesis. Mass. Inst. Technol.

139. Richards-Kortum R, Rava RP, Fitzmaurice M, Kramer JR, Feld MS. 1991. *Am. Heart J.* 122:1141–50

140. Richards-Kortum R, Mehta A, Hayes G, Cothren R, Kolubayev T, et al. 1989. *Am. Heart J.* 118:381–91

141. Hoyt CC, Richards-Kortum R, Costello B, Sacks BA, Kittrell C, et al. 1988. *Lasers Surg. Med.* 8:1–9

142. Warren S, Pope K, Yazdi Y, Welch AJ, Thomsen S, et al. 1995. *IEEE Trans. Biomed. Eng.* 42:121–32

143. Chaudhry HW, Richards-Kortum R, Kolubayev T, Kittrell C, Partovi F, et al. 1989. *Lasers Surg. Med.* 9:572–80

144. Morguet AJ, Korber B, Abel B, Hippler H, Wiegand V, Kreuzer H. 1994. *Lasers Surg. Med.* 14:238–48

145. Papazoglou TG, Papaioannou T, Arakawa K, Fishbein M, Marmarelis VZ, Grundfest WS. 1990. *Appl. Opt.* 29:4950–55

146. Lycette RM, Leslie RB. 1965. *Lancet* 2:436

147. Alfano RR, Tata DB, Cordero J, Tomashefsky P, Longo FW, Alfano MA. 1984. *IEEE J. Quantum Electron.* 20:1507–11

148. Yuanlong Y, Yanming Y, Fuming L, Yufen L, Paozhong M. 1987. *Lasers Surg. Med.* 7:528–32

149. Richards-Kortum R, Rava RP, Petras RE, Fitzmaurice M, Sivak M, Feld MS. 1991. *Photochem. Photobiol.* 53:777–86

150. Kapadia CR, Cutruzzola FW, O'Brien

KM, Stetz ML, Enriquez R, Deckelbaum LI. 1990. *Gastroenterology* 93:150–57

151. Schomacker KT, Frisoli JK, Compton CC, Flotte TJ, Richter JM, et al. 1992. *Gastroenterology* 102:1155–60

152. Schomacker K, Frisoli JK, Compton CC, Flotte TJ, Richter J, et al. 1992. *Lasers Surg. Med.* 12:63–78

153. Cothren RM, Richards-Kortum R, Sivak MV, Fitzmaurice M, Rava RP, et al. 1990. *Gastrointest. Endosc.* 36:105–11

154. Cothren R, Sivak M, Van Dam J, Petras RE, Fitzmaurice M, Crawford JM, Brennan JF, Rava RP, Manoharan R, Feld MS. 1996. *Gastrointest. Endosc.* In press

155. Romer TJ, Fitzmaurice M, Cothren R, Richards-Kortum R, Petras R, et al. 1995. *Am. J. Gastroenterol.* 90:81–87

156. Bottiroli G, Croce AC, Locatelli D, Marchesini R, Pignoli E, et al. 1995. *Lasers Surg. Med.* 16:48–60

157. Fiarman GS, Nathanson MH, West AB, Deckelbaum LI, Kelly L, Kapadia CR. 1995. *Dig. Dis. Sci.* 40:1261–68

158. Manoharan R, Zonios G, Cothren R, Arendt J, Van Dam J, Feld MS. 1995. *Proc. SPIE* 2388:47–22

159. Lohmann W, Mussmann J, Lohmann C, Kunzel W. 1989. *Eur. J. Obstet. Gynecol. Reprod. Biol.* 31:249–53

160. Glassman WS, Liu CH, Tang GC, Lubicz S, Alfano RR. 1992. *Lasers Life Sci.* 5:49–58

161. Glassman WS, Liu CH, Lubicz S, Alfano RR. 1994. *Lasers Life Sci.* 6:99–106

162. Mahadevan A, Mitchell M, Silva E, Thomsen S, Richards-Kortum RR. 1993. *Lasers Surg. Med.* 13:647–55

163. Ramanujam N, Mitchell MF, Mahadevan A, Thomsen S, Silva E, Richards-Kortum RR. 1994. *Gynecol. Oncol.* 52:31–38

164. Ramanujam N, Mitchell MF, Mahadevan A, Thomsen S, Richards-Kortum RR. 1994. *Proc. Natl. Acad. Sci. USA* 91:10193–97

165. Mitchell MF. 1994. *Clin. Consult. Obstet. Gynecol.* 6(1):70–73

166. Ramanujam N, Mitchell MF, Mahadevan A, Thomsen S, Malpica A, et al. 1996. *Lasers Surg. Med.* In press

167. Ramanujam N, Mitchell MF, Mahadevan A, Thomsen S, Malpica A, et al. 1996. *Lasers Surg. Med.* In press

168. Ramanujam N, Mitchell MF, Mahadevan A, Thomsen S, Malpica A, et al. 1996. *Photochem. Photobiol.* Submitted

169. Alfano RR, Tang GC, Pradhan A, Lam W, Choy DSJ, Opher E. 1987. *IEEE J. Quantum Electron.* 23:1806–11

170. Alfano RR, Pradhan A, Tang GC. 1989. *J. Opt. Soc. Am. B* 6:1015–23

171. Glassman WS, Steinberg M, Alfano RR. 1994. *Lasers Life Sci.* 6:91–98

172. Lohmann W, Kunzel S, Mussmann J, Hoersch C. 1990. *Naturwissenschaften* 77:476–78

173. Lohmann W, Bodecker RH. 1991. *Naturwissenschaften* 78:456–57

174. Sterenborg HJCM, Motamedi M, Wagner RF, Duvic M, Thomsen S, Jacques SL. 1994. *Lasers Med. Sci.* 9:191–201

175. Zeng H, MacAulay C, Palcic B, McLean D. 1993. *Proc. SPIE* 1876:129–35

176. Lohmann W, Paul E. 1989. *Naturwissenschaften* 76:424–26

177. Zeng H, MacAulay C, Palcic B, McLean D. 1993. *Phys. Med. Biol.* 38:231–40

178. Zeng H, MacAulay C, Palcic B, McLean D. 1993. *Proc. SPIE* 1882:278–90

179. Roy K, Bottrill ID, Ingrams DR, Pankratov MM, Rebeiz EE, et al. 1995. *Proc. SPIE* 2395:135–42

180. Konig K, Schneckenburger H. 1994. *J. Fluoresc.* 4:17–40

181. Glasgold R, Glasgold M, Savage H, Pinto J, Alfano R, Schantz S. 1994. *Cancer Lett.* 82:33–41

182. Silverberg M, Savage H, Tang G, Sacks P, Alfano R, Schantz S. 1994. *Laryngoscope* 104:278–82

183. Savage H, Kolli V, Ansley J, Chandawarkar R, Alfano R, Schantz S. 1995. *Proc. SPIE* 2387:2–9

184. Kluftinger AM, Quenville NF, Lam S, Hung J, Palcic B. 1992. *Surg. Oncol.* 1:183–88

185. D'Hallewin MA, Baert L, Vanherzeele. 1994. *J. Am. Paraplegia Soc.* 17:161–64

186. Hung J, Lam S, LeRiche J, Palcic B. 1991. *Lasers Surg. Med.* 11:9–105

187. Harries M, Lam S, MacAulay C, Qu J, Palcic B. 1995. *J. Laryngol. Otol.* 109:108–10

188. Lohmann W, Hirzinger B, Braun J, Schwemmle K, Muhrer K, Schulz A. 1990. *Z. Naturforsch.* 45C:1063–66

189. Palcic B, Lam S, Hung J, MacAulay C. 1991. *Chest* 99:742–43

190. Lam S, MacAulay C, Hung J, LeRiche J, Profio AE, Palcic B. 1993. *J. Thorac. Cardiovasc. Surg.* 105:1035–40

191. Avrillier S, Hor F, Desgeorges M, Ettori D, Sitbon J. 1993. *Proc. SPIE* 1894:177–86

192. Montan S, Stromblad LG. 1987. *Lasers Life Sci.* 1:275–85

193. Mordon S, Devoisselle JM, Maunoury V. 1994. *Photochem. Photobiol.* 60:274–79

194. Russell DA, Pottier RH, Valenzeno DP. 1994. *Photochem. Photobiol.* 59:309–13

195. Ahmed SA, Zhang KW, Yoo KM, Ali A, Alfano RR. 1994. *Appl. Opt.* 33:2746–50

196. Andreoni A. 1990. *Photochem. Photobiol.* 52:423–30

197. Moan J, Sommer S. 1984. *Photochem. Photobiol.* 40:631–34

198. Tanielian C, Heinrich G. 1995. *Photochem. Photobiol.* 61:131–35

199. Nilsson H, Johansson J, Svanberg K, Svanberg S, Jori G, et al. 1994. *Br. J. Cancer* 70(5):873–79

200. Svanberg K, Kjellen E, Ankerst J, Montan S, Sjöholm E, Svanberg S. 1986. *Cancer Res.* 46:3803–8

201. Andersson-Engels S, Ankerst J, Johansson J, Svanberg K, Svanberg S. 1989. *Laser Med. Sci.* 4:115–23

202. Andersson-Engels S, Ankerst J, Johansson J, Svanberg K, Svanberg S. 1993. *Photochem. Photobiol.* 57:978–83

203. Van Leengoed HLLM, Van Der Veen N, Verteeg AAC, Van Der Berg-Blok AE, Marijnissen JPA, Star WM. 1991. *Int. J. Radiat. Biol.* 60:121–24

204. Andersson-Engels S, Johansson J, Stenram U, Svanberg K, Svanberg S. 1993. *J. Photochem. Photobiol. B* 4:363–69

205. Ye BQ, Abela GS. 1993. *Lasers Med. Surg.* 13:393–404

206. Green HA, Bua D, Anderson R, Nishioka NS. 1992. *Arch. Dermatol.* 128:43–49

207. Haugland RP. 1992. *Molecular Probes, Inc.* Eugene, OR (Catalog)

208. Pottier R. 1990. *Photobiol. B* 6(1–2):103–9

209. Biolo R, Jori G, Kennedy JC, Nadeau P, Pottier R, et al. 1991. *Photochem. Photobiol.* 53:113–18

210. Panjehpour M, Sneed RE, Frazier DL, Barnhill MA, O'Brien SF, et al. 1993. *Lasers Surg. Med.* 13:23–10

211. Blasdel GC, Salama G. 1986. *Nature* 321:579–84

212. Ando T, Irie K, Koshimizu K, Takemura T, Nishino H, Iwashima A. 1993. *Photochem. Photobiol.* 57:629–33

213. Marriott G, Clegg RM, Arndt-Jovin DJ, Jovin TM. 1991. *Biophys. J.* 60:1374–87

214. Oida T, Sako Y, Kusumi A. 1993. *Biophys. J.* 64:676–85

215. Schneckenburger H, Konig K, Dienersberger T, Hahn R. 1994. *Opt. Eng.* 33:2600–6

216. Lakowicz JR, Szmacinski H, Nowaczyk K, Berndt KW, Johnson M. 1992. *Anal. Biochem.* 202:316–30

217. Sanders R, Draaijer A, Gerritsen HC, Houpt PM, Levine YK. 1995. *Anal. Biochem.* 227:302–8

218. Lakowicz JR, Szmacinski H, Nowaczyk K, Johnson ML. 1992. *Proc. Natl. Acad. Sci. USA* 89:1271–75

219. Andersson-Engels S, Johansson J, Stenram U, Svanberg K, Svanberg S. 1990. *IEEE J. Quantum Electron.* 26:2207–17

220. Baraga JJ, Taroni P, Park YD, An K, Macstri A, et al. 1989. *Spectrochim. Acta* 45A:95–99

221. Tata DB, Foresti M, Cordero J, Tomashefpsky P. 1986. *Biophys. J.* 50:463–69

222. Dillon J, Atherton SJ. 1990. *Photochem. Photobiol.* 51:465–68

223. Konig K, Schneckenburger H, Hemmer J, Tromberg B, Steiner R. 1994. *Proc. SPIE* 2135:129–38

224. Cubeddu R, Ramponi R, Taroni P Canti G. 1991. *J. Photochem. Photobiol. B. Biol.* 11:319–28

225. Cubeddu R, Canti G, Taroni P, Valentini G. 1993. *Photochem. Photobiol.* 57:480–85

226. Seidlitz HK, Schneckenburger H, Stettmaier K. 1990. *J. Photochem. Photobiol. B* 5:391–400

227. Cubeddu R, Ramponi R, Bottiroli G. 1986. *Chem. Phys. Lett.* 128:439–42

228. Valduga G, Reddi E, Jori G, Cubeddu R, Taroni P, Valentini G. 1992. *J. Photochem. Photobiol. B* 16:331–40

229. Ambroz M, MacRobert AJ, Morgan J, Rumbles G, Foley MSC, Phillips D. 1994. *J. Photochem. Photobiol. B* 22:105–17

230. Seidlitz HK, Stettmaier K, Wessels JM, Schneckenburger H. 1992. *Opt. Eng.* 31:1482–86

231. Konig K, Wabnitz H, Dietel W. 1990. *J. Photochem. Photobiol.* 8(1):103–11

232. Konig K, Schneckenburger H, Ruck A, Steiner R. 1993. *J. Photochem. Photobiol.* 18(2–3):287–90

233. van Leengoed HLLM, van der Veen N, Versteeg AAC, Ouellet R, van Lier JE, Star WM. 1993. *Photochem. Photobiol.* 58:233–37

234. Vanderkooi JM, Maniara G, Green TJ, Wilson DF. 1987. *J. Biol. Chem.* 262:5476–82

235. Vanderkooi JM, Wilson DF. 1986. *Adv. Exp. Med. Biol.* 200:189–93

236. Rumsey WL, Vanderkooi JM, Wilson DF. 1989. *Science* 241:1649–51

237. Wilson DF. 1993. In *Optical Imaging of Brain Function and Metabolism,* ed. U Dirnagl, A Villringer, KM Einnaupl, pp. 225–32. New York: Plenum

238. Torres F, Leunig M, Yuan F, Intaglietta M, Jain R. 1994. *Proc. Natl. Acad. Sci. USA* 91:2081–85

239. Bachteler G, Drexhage KH, Arden-Jacob J, Han KT, Kollner M, et al. 1994. *J. Lu-*

min. 62:101–8

240. Bachteler G, Drexhage KH, Arden-Jacob J, Han KT, Kollner M, et al. 1994. *J. Lumin.* 60&61:511–14

241. Carey PR. 1982. *Biochemical Applications of Raman and Resonance Raman Spectroscopies.* New York: Academic

242. Parker FS. 1983. *Applications of Infrared, Raman, and Resonance Raman Spectroscopy in Biochemistry.* New York: Plenum

243. Twardowski J, Anzenbacher P. 1994. *Raman and IR Spectroscopy in Biology and Biochemistry.* New York: Ellis Horwood

244. Ozaki Y. 1988. *Appl. Spectrosc. Rev.* 24(3&4):259–312

245. Nie S, Bergbauer KJ, Ho JJ, Kuck JFR Jr, Yu NT. 1990. *Spectroscopy* 5:24–32

246. Schrader B, Keller S, Loechte T, Fendel S, Moore DS, Simon A. 1995. *J. Mol. Struct.* 348:293–96

247. Manoharan R, Baraga JJ, Rava RP, Dasari RR, Fitzmaurice M, Feld MS. 1993. *Atherosclerosis* 103(2):181–93

248. Liu CH, Das BB, Glassman WL, Tang GC, Yoo KM, et al. 1992. *J. Photochem. Photobiol. B* 16:187–209

249. Feld MS, Manoharan R, Salenius J, Orenstein-Carndona J, Romer TJ, et al. 1995. In *Advances in Fluorescence Sensing Technology II,* ed. JR Lakowicz, 2388:99–104. Bellingham: SPIE

250. Frank CJ, McCreery RL, Redd DCB. 1995. *Anal. Chem.* 67(5):777–83

251. Mahadevan Jansen A, Mitchell MF, Ramanujam N, Malpica A, Thomsen S, Richards-Kortum R. 1996. *Appl. Spectrosc.* Submitted

252. Yada RY, Jackman RL, Nakai S. 1988. *Int. J. Peptide Protein Res.* 31(1):98–108

253. Peticolas WL, Evertsz E. 1992. *Methods Enzymol.* 211:335–52

254. Duguid J, Bloomfield VA, Benevides J, Thomas GJ Jr. 1993. *Biophys. J.* 65(5):1916–28

255. Kennard O, Hunter WN. 1989. *Q. Rev. Biophys.* 22(3):327–79

256. Steitz TA. 1990. *Q. Rev. Biophys.* 23(3):205–80

257. Hud NV, Milanovich FP, Balhorn R. 1994. *Biochemistry* 33(24):7528–35

258. Aubrey KL, Casjens SR, Thomas GJ Jr. 1992. *Biochemistry* 31(47):11835–42

259. Puppels GJ, Olminkhof JH, Segers-Nolten GM, Otto C, deMul FF, Greve J. 1991. *Exp. Cell Res.* 195(2):361–67

260. Puppels GJ, Garritsen HS, Segers-Nolten GM, de Mul FF, Greve J. 1991. *Biophys. J.* 60(5):1046–56

261. Yu NT, East EJ. 1975. *J. Biol. Chem.* 250:2196–202

262. Clarke RH, Hanlon EB, Isner JM, Brody H. 1987. *Appl. Opt.* 26(16):3175–77

263. Baraga JJ, Feld MS, Rava RP. 1992. *Appl. Spectrosc.* 46(2):187–90

264. Manoharan R, Wang Y, Boustany N, Brennan JF III, Baraga JJ, et al. 1994. *Proc. Biomed. Optoelectron. Devices Systems II, SPIE* 2328:128–32

265. Mahadevan A, Ramanujam N, Mitchell MF, Malpica A, Thomsen S, Richards-Kortum R. 1995. In *Advances in Fluorescence Sensing Technology II,* ed. JR Lakowicz, 2388:110–20. Bellingham: SPIE

266. Mosier-Boss PA, Lieberman SH, Newberry R. 1995. *Appl. Spectrosc.* 49(5):630–38

267. Angel SM, DeArmond MK, Hanck KW, Wertz DW. 1984. *Anal. Chem.* 56:3000–1

268. Funfschilling J, Williams DF. 1976. *Appl. Spectrosc.* 30(4):443–46

269. Shreve AP, Cherepy NJ, Mathies RA. 1992. *Appl. Spectrosc.* 46(4):707–11

270. Bot ACC. 1989. *Exp. Eye Res.* 49:161–69

271. Redd DCB, Feng ZC, Yue KT, Gansler TS. 1993. *Appl. Spectrosc.* 47(6):787–91

272. Keller S, Schrader B, Hoffmann A, Schrader W, Metz K, et al. 1994. *J. Raman Spectrosc.* 25(7–8):663–71

273. Richards-Kortum R, Mahadevan A, Ramanujam N. 1996. Unpublished data

274. Yu NT, DeNagel DC, Pruett PL, Kuck JFR Jr. 1985. *Proc. Natl. Acad. Sci. USA* 82:7965–68

275. Williams AC, Barry BW, Edwards HG. 1994. *Analyst* 119(4):563–66

276. Manoharan R, Wang Y, Dasari RR, Singer S, Rava RP, Feld MS. 1995. *Lasers Life Sci.* 6(4):217–27

277. Alfano RR, Lui CH, Sha WL, Zhu HR, Akins DL, et al. 1991. *Lasers Life Sci.* 4(1):23–28

278. Frank CJ, Redd DC, Gansler TS, McCreery RL. 1994. *Anal. Chem.* 66(3):319–26

279. Mizuno A, Kitajima H, Kawauchi K, Muraishi S, Ozaki Y. 1994. *J. Raman Spectros.* 25:25–29

280. Lim HW, Soter NA. 1993. *Clinical Photomedicine.* New York: Dekker

281. Giuntoli RL, Atkinson BF, Ernst CS, Rubin MM, Egan VS. 1987. *Cytology and Histopathology.* Philadelphia: Lippincott & Co.

282. Schneckenburger H, Konig K. 1992. *Opt. Eng.* 31:1447–51